AGU PUBLICATIONS

Geochemistry, Geophysics, Geosystems

RESEARCH ARTICLE

10.1002/2017GC007296

Key Points:
- The summit crater Voragine at Etna volcano produced exceptional powerful eruptions in December 2015 and May 2016
- Geophysical and petrological data led us to constrain chemically, physically, and kinetically the magma storage and transfer dynamics
- Fast magma transfer from deep environments is the main factor leading to reawakening of explosive activity at the Voragine crater

Supporting Information:
- Supporting Information S1
- Data Set S1
- Data Set S2
- Data Set S3
- Data Set S4

Correspondence to:
A. Cannata,
andrea.cannata@unipg.it;
M. Palano,
mimmo.palano@ingv.it;
M. Viccaro,
m.viccaro@unict.it

Citation:
Cannata, A., Di Grazia, G., Giuffrida, M., Gresta, S., Palano, M., Sciotto, M., et al. (2018). Space-time evolution of magma storage and transfer at Mt. Etna volcano (Italy): The 2015–2016 reawakening of Voragine crater. *Geochemistry, Geophysics, Geosystems*, *19*. https://doi.org/10.1002/2017GC007296

Received 20 OCT 2017
Accepted 1 FEB 2018
Accepted article online 9 FEB 2018

Space-Time Evolution of Magma Storage and Transfer at Mt. Etna Volcano (Italy): The 2015–2016 Reawakening of Voragine Crater

Andrea Cannata[1,2], Giuseppe Di Grazia[2], Marisa Giuffrida[3], Stefano Gresta[3], Mimmo Palano[2], Mariangela Sciotto[2], Marco Viccaro[2,3], and Francesco Zuccarello[3]

[1]Dipartimento di Fisica e Geologia, Piazza Università, Università degli Studi di Perugia, Perugia, Italy, [2]Istituto Nazionale di Geofisica e Vulcanologia - Sezione di Catania, Osservatorio Etneo, Catania, Italy, [3]Dipartimento di Scienze Biologiche, Geologiche e Ambientali - Sezione di Scienze della Terra, Università degli Studi di Catania, Catania, Italy

Abstract The eruptions of December 2015 and May 2016 at Voragine crater were among the most explosive recorded during the last two decades at Mt. Etna volcano. Here we present data coming from geophysics (infrasound, LP, VLP, volcanic tremor, VT earthquakes, and ground deformations) and petrology (textural and microanalytical data on plagioclase and olivine crystals) to investigate the preeruptive magma storage and transfer dynamics leading to these exceptional explosive eruptions. Integration of all the available data has led us to constrain chemically, physically, and kinetically the environments where magmas were stored before the eruption, and how they have interacted during the transfer en-route to the surface. Although the evolution and behavior of volcanic phenomena at the surface was rather similar, some differences in storage and transfer dynamics were observed for 2015 and 2016 eruptions. Specifically, the 2015 eruptions have been fed by magmas stored at shallow levels that were pushed upward as a response of magma injections from deeper environments, whereas evidence of chemical interaction between shallow and deep magmatic environments becomes more prominent during the 2016 eruptions. Main findings evidence the activation of magmatic environments deeper than those generally observed for other recent Etnean eruptions, with involvement of deep basic magmas that were brought to shallow crustal levels in very short time scales (~1 month). The fast transfer from the deepest levels of the plumbing system of basic, undegassed magmas might be viewed as the crucial triggering factor leading to development of exceptionally violent volcanic phenomena even with only basic magma involved.

1. Introduction

Improvements in volcanic hazard assessment require the enhancement of our knowledge on the structure, geometry, magma dynamics, and time scales in the plumbing system. To this aim, a multidisciplinary approach, consisting in integrating and analyzing information coming from multidisciplinary data sets is strictly recommended (e.g., Pallister & McNutt, 2015).

Subsurface fluid (i.e., magma, volatiles, or hydrothermal waters) movements produce ground deformations that can be measured on the volcano surface: modeling of these deformations is performed worldwide in order to achieve constraints about geometry, size, and depth range of magmatic reservoirs as well as about fluid migration within active volcanoes (e.g., Dzurisin, 2007). Volcanoes also generate different types of seismic signals attributed to both fluid dynamics within the plumbing system and rock shear failure or slip on faults. The study of these signals can shed light on the structure of the shallower portions of plumbing system (Chouet & Matoza, 2013, and references therein), on the magmatic intrusions (e.g., Tarasewicz et al., 2014), and on processes taking place within the plumbing system, such as pressurization and depressurization (e.g., Cannata et al., 2015). Infrasound complements volcano seismic monitoring and research in its capability to robustly detect and characterize near-surface activity (e.g., McNutt et al., 2015). Indeed, it has been used to provide information about the geometry of the uppermost portions of the plumbing system (e.g., Sciotto et al., 2013), to investigate its modifications during the eruptions (Fee et al., 2017), as well as to reconstruct the evolution of the eruptive (especially explosive) activities (e.g., Ripepe et al., 2013). Other insights into the dynamics and timing of magma storage and transfer can be provided by petrological data,

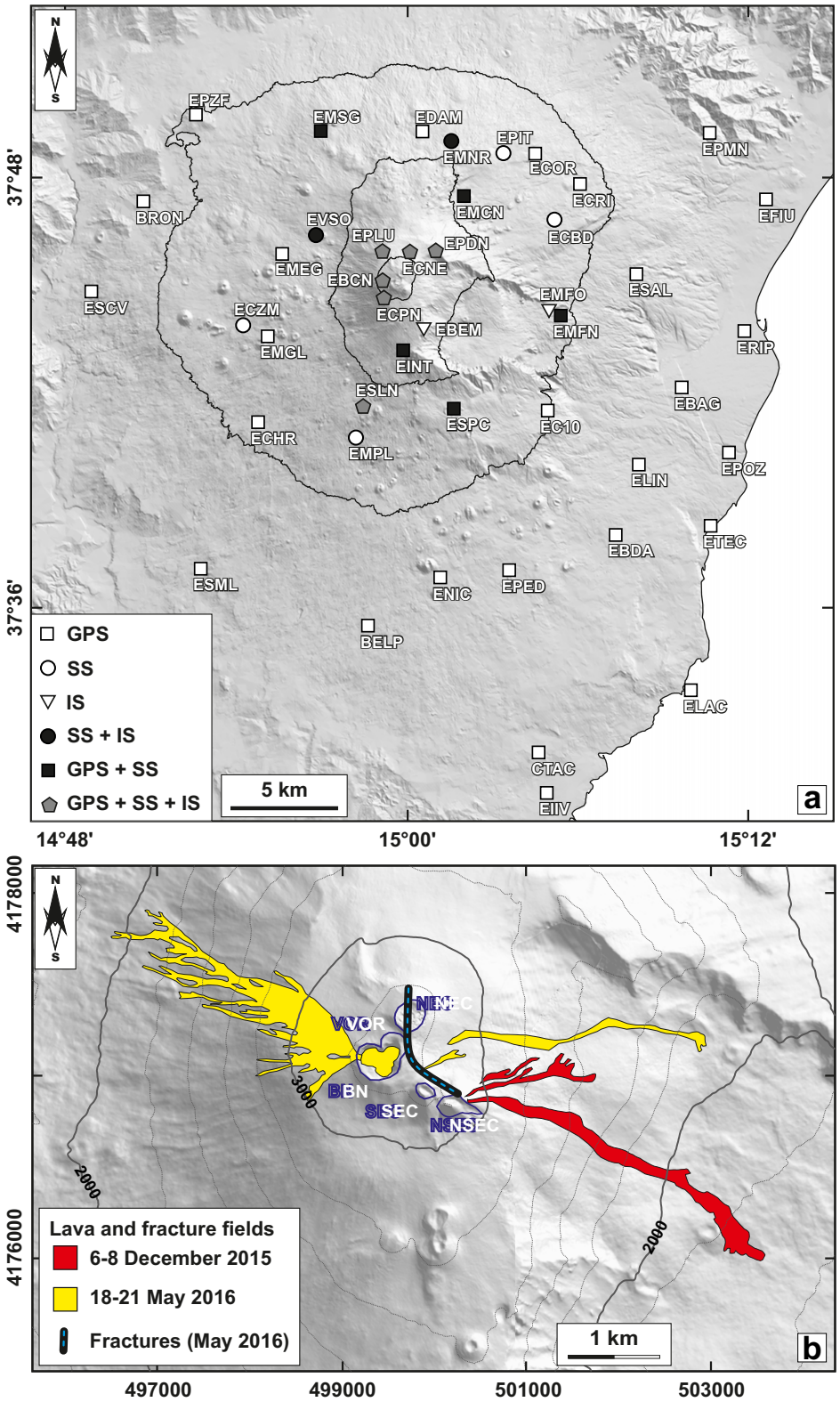

Figure 1. (a) Map of Mount Etna volcano with the location of the seismic (SS), infrasound (IS), and geodetic (GPS) stations. Note that in the upper portion of the volcano, many of the stations are colocated (see the map legend). (b) Enlargement of the volcano summit craters (Bocca Nuova, BN; Voragine, VOR; North-East Crater, NEC; South-East Crater, SEC; New South-East Crater, NSEC) and eruptive fissures and vents opened during the analyzed period.

taking into account mineral phases sensitive to changes in the thermodynamic equilibrium of the magmatic system, such as plagioclase and olivine (Davidson et al., 2001, 2007; Druitt et al., 2012; Kahl et al., 2011).

Mt. Etna, an open-vent Quaternary basaltic volcano located on the eastern coast of Sicily (Figure 1a), can be considered an excellent natural laboratory to perform integrations of such distinct types of data and carry out multidisciplinary studies (e.g., Cannata et al., 2015; Gambino et al., 2016; Spampinato et al., 2015; Viccaro et al., 2016a). Indeed, it is a very active volcano that has been characterized by numerous intense explosive and effusive eruptions in the last decade, thus providing volcanic products to carry out petrological studies. Furthermore, Etna is monitored by one of the densest multiparametric permanent networks worldwide, continuously producing streaming of varied data (i.e., seismic, infrasonic, GPS, tiltmetric, gravimetric, video, and thermal; e.g., Patanè et al., 2013).

Mt. Etna volcano is currently characterized by five summit craters (Figure 1b). The New South-East Crater (NSEC) is the youngest one being formed in 2006; South-East Crater (SEC) in 1971 as a pit crater, being eruptive in 1978; Bocca Nuova (BN) in 1968; North-East Crater (NEC) in 1911; Voragine (VOR), is the oldest among them, being represented in the iconography since the fourteenth century. Its paroxysmal eruptive activity is rare but very powerful; its two 1 day long eruptions of 22 July 1998 and 4 September 1999 have been ranked among the most powerful summit eruptions at Mt. Etna in the whole past century (i.e., Corsaro et al., 2017). For example, during 2011–2014, NSEC produced more than 50 paroxysmal episodes, while SEC, BN, NEC, experienced a mild activity (e.g., Behncke et al., 2014; Corsaro et al., 2017; Giuffrida & Viccaro, 2017). On the contrary, the paroxysmal eruptions affecting VOR during 2015–2016 were the first ones since 1999. Four eruptions took place on 3–5 December, which were accompanied by vigorous lava fountaining up to 2 km above the crater edge and development of pyroclastic columns 10–14 km on the volcano top. Again, on 18–19 May 2016 two lava fountain eruptions occurred at VOR crater, accompanied by the emplacement of short-living lava flows (e.g., Corsaro et al., 2017). Bonaccorso and Calvari (2017) have analyzed in detail the 7 days time span encompassing the 3–5 December 2015 eruptions at VOR, by using borehole strainmeters and cameras data.

The aim of this paper is to investigate, during a broader time span (June 2015 to August 2016), the volcano internal processes that led to these powerful eruptions at VOR crater. Then, we will provide petrological data related to the products emitted from VOR during such a period, integrating them with ground deformations, seismic and infrasonic data. The combined analyses of these whole data sets will enlighten the spatial and temporal dynamics of magma storage and transport into the Etnean plumbing system. Some factors able to produce exceptional explosive eruptions after a prolonged period of rest will be suggested.

2. Volcanological Background

During June–July 2015, the Etna summit craters were characterized by quiet degassing, while since mid-August an increasing steaming, coupled with sporadic, low-energy ash emissions started at VOR crater (Figure 2a). Since mid-November 2015, mild Strombolian activity was observed at the bottom of VOR. Such activity gradually intensified in the next few weeks and was coupled with episodic gas (mostly vapor) emission from a fumarolic area on the upper eastern flank of NSEC (Corsaro et al., 2017). On 25 November, the fumarolic area collapsed and led to the formation of a circular 50 m-wide vent, which started to produce a weak Strombolian activity and intense gas emissions. Activity at the VOR showed a marked increase during late November. On the evening of 2 December 2015, Strombolian explosions at VOR were almost continuous, and the activity increased in the following hours, marking the beginning of a rapid sequence of summit eruptive episodes mainly involving craters VOR and NSEC, at different times. In particular, during 3–5 December, VOR produced four powerful paroxysmal episodes with eruption columns up to 10–14 km asl and no lava flows emission (Corsaro et al., 2017). In the following days, weak to moderately intense ash emissions occurred nearly continuously from both VOR and NEC (Figure 2a). From 6 December up to 8 December, eruptive activity (Figure 2a) involved also the vent opened on the upper eastern flank of NSEC with the formation of some small lava flows advancing toward the Valle del Bove (Figure 1b). In addition, between 7 and 10 December 2015, an intense seismic swarm (about 100 earthquakes with local maximum magnitude Ml = 3.6) occurred along the uppermost segment of the Pernicana-Provenzana fault system (Aloisi et al., 2017). In the following weeks, weak ash emissions occurred at NSEC, NEC, and VOR craters.

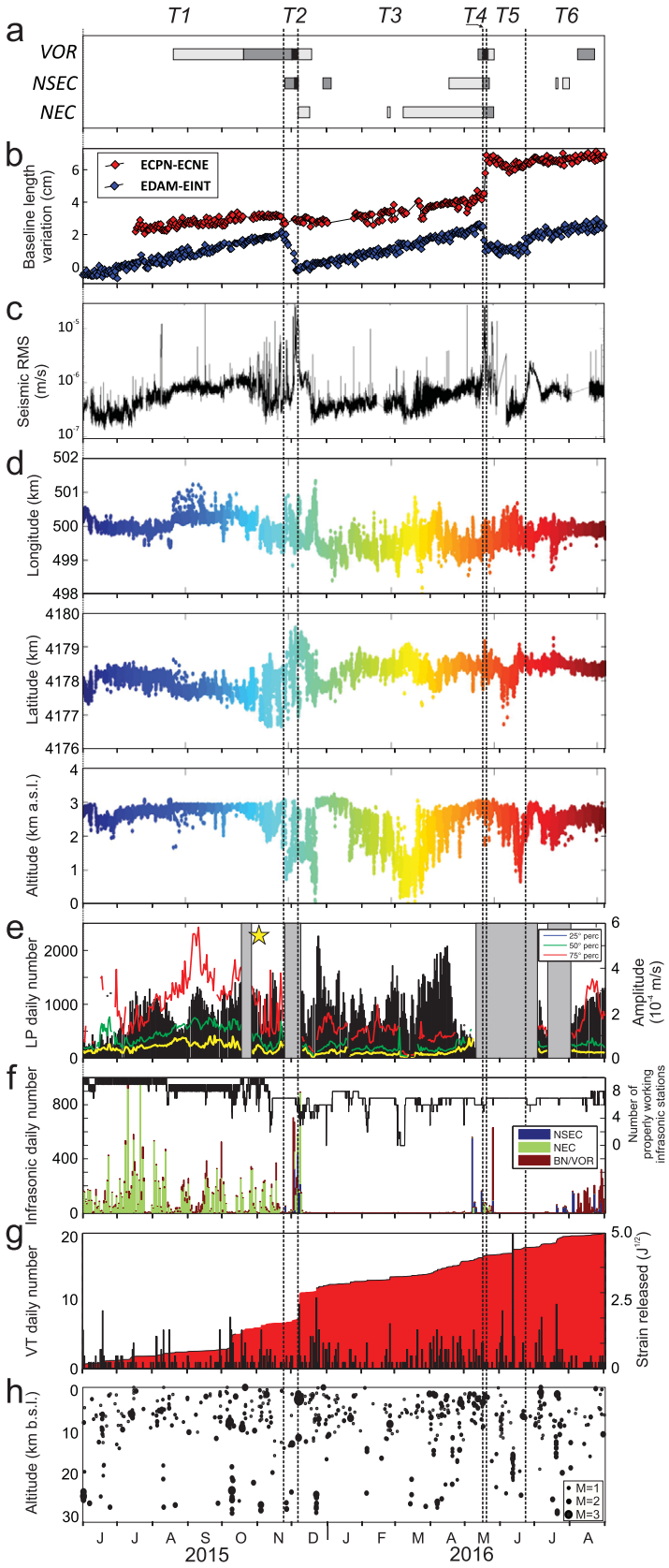

Figure 2. (continued)

Since early January 2016, the summit craters of the volcano were characterized by a quiet degassing, while some intermittent and weak ash emissions occurred in late February at NEC and in late March both at NSEC and NEC (Figure 2a). On late 17 May 2016, Strombolian activity started at NEC, while on middle 18 May, a lava fountaining episode started at VOR (Figure 2a). During this last event, a 400 m-wide fracture field opened from the northern flank of NEC up to SEC, crossing the whole summit area, with a prevailing N-S orientation on the northern and central portions, and a NW-SE attitude on the southern portion (Figure 1b). The lava fountaining episode led also to the formation of two lava flows: one emitted from BN crater and advancing westward on the western slope of the volcano and the other, emitted from a vent opened at the eastern side of NEC and advancing toward Valle del Bove (Figure 1b). On early 19 May, a new lava fountaining episode took place at VOR, accompanied by the occurrence of another lava flow that, flowing from BN and advancing westward, overlapped the lava field emitted the day before. On 21 May, a third lava fountaining episode took place at VOR, which was accompanied by a lava overflow that superimposed to the flow of 19 May and by another lava flow poured out by a fissure opened at the northern base of the NSEC. The Strombolian activity affected the NSEC and NEC until 26 May. The following weeks were characterized by degassing from the summit craters up to mid-July 2016, when mild explosive activities resumed at NSEC and, successively, at VOR.

3. Geophysical Data

As mentioned above, the main eruptive episodes analyzed in this study occurred in December 2015 and in May 2016. However, in order to contextualize these eruptive episodes within the framework of a longer time interval, all the available geophysical data spanning the June 2015 to August 2016 interval have been analyzed. This provides a comprehensive picture of events leading up to these episodes.

3.1. Geodetic Data

Raw data collected from the permanent GPS network (Figure 1a) and spanning the 1 June 2015 to 31 August 2016 interval were analyzed

Figure 2. Summary of the eruptive activity, seismic, and deformation data from June 2015 to August 2016. (a) Sketch showing the eruptive periods at VOR, NSEC, and NEC (light grey: weak ash emission; dark grey: Strombolian activity; black: lava fountain). (b) Variation in length of the EDAM-EINT and ECPN-ECNE baselines. T1–T6 are time intervals discussed in the text. (c) RMS amplitudes of the seismic signal recorded by the vertical component of ESLN station and filtered in the band 0.5–5.5 Hz. (d) Variation in time of the centroid locations of volcanic tremor source (colors change over time). (e) Daily number (histogram) and amplitude (lines) of LP events. In particular, yellow, green, and red lines indicate time series of the daily 25°, 50°, and 75° percentile, respectively, calculated on the event peak-to-peak amplitudes. The yellow star indicates the time of occurrence of the strong LP event taking place on 1 November 2015. (f) Stacked histogram showing the daily number of infrasonic events located in NSEC, NEC, and VOR/BN areas (see the legend). The black line exhibits the variation over time of the number of properly working infrasonic stations. (g) VT earthquake daily number (black histogram) and cumulative strain release (x105, red area). (h) Variation in time of the depth of the VT earthquakes. The size of the dots is proportional to the event magnitude (see legend in the right bottom corner).

using the GAMIT/GLOBK software (Herring et al., 2015) following the methodology described in Gonzalez and Palano (2014). The GAMIT daily solutions were used as input in a Kalman filter (GLOBK) in order to estimate a consistent set of daily coordinates (i.e., time series) for all sites involved.

To detect significant signals related to Mt. Etna activity, we analyzed the daily baseline changes for some selected sites. Among the available sites, we focus on EDAM and EINT stations because they were quasi-continuously operating throughout the investigated period (Figures 1a and 2b). These stations are located north (EDAM) and south (EINT) of the summit area, hence their relative motion over time is sensitive to any change in the Mt. Etna plumbing system. In addition, in order to capture deformation signal related to the opening of the fracture field related to the May 2016 lava fountaining episodes, we considered also the daily baseline changes for ECPN and ECNE stations (Figures 1 and 2b). A total of six major ground deformation stages are apparent in the EDAM-EINT baseline time series (Figure 2b): (T1) from 1 July 2015 to 2 December 2015, the baseline lengthened by ~3.0 cm; (T2) from 2 December to 9 December 2015, the baseline shortened by ~2.3 cm; (T3) from 9 December 2015 to 17 May 2016, the baseline lengthened by ~2.8 cm; (T4) from 17 May to 20 May, the baseline shortened by ~1.6 cm. During this last ground deformation stage, the ECPN-ECNE baseline lengthened by ~2.2 cm, marking the opening of the shallow fracture field in concomitance with the lava fountaining episode at VOR on 18 May (see also supporting information Figure S1). After some few weeks of no significant ground deformation (T5), since 20 June 2016 (T6), the baseline lengthened again (with different rates), marking the beginning of a new pressurization phase of the volcano plumbing system. In the following, we focused on T1, T2, T3, and T4 deformation stages because they are strictly related to the main eruptive episodes occurred in December 2015 and in May 2016. Although these stages have been delineated only on the basis of deformation pattern, in the following we refer to them, because of the strict temporal relation between deformation, volcanic activity, seismo-volcanic, and infrasonic signals.

For each detected stage, we estimated the ground deformation field in terms of geodetic velocities by combining the daily GAMIT solutions into a consistent set of station positions and velocities and adopting a

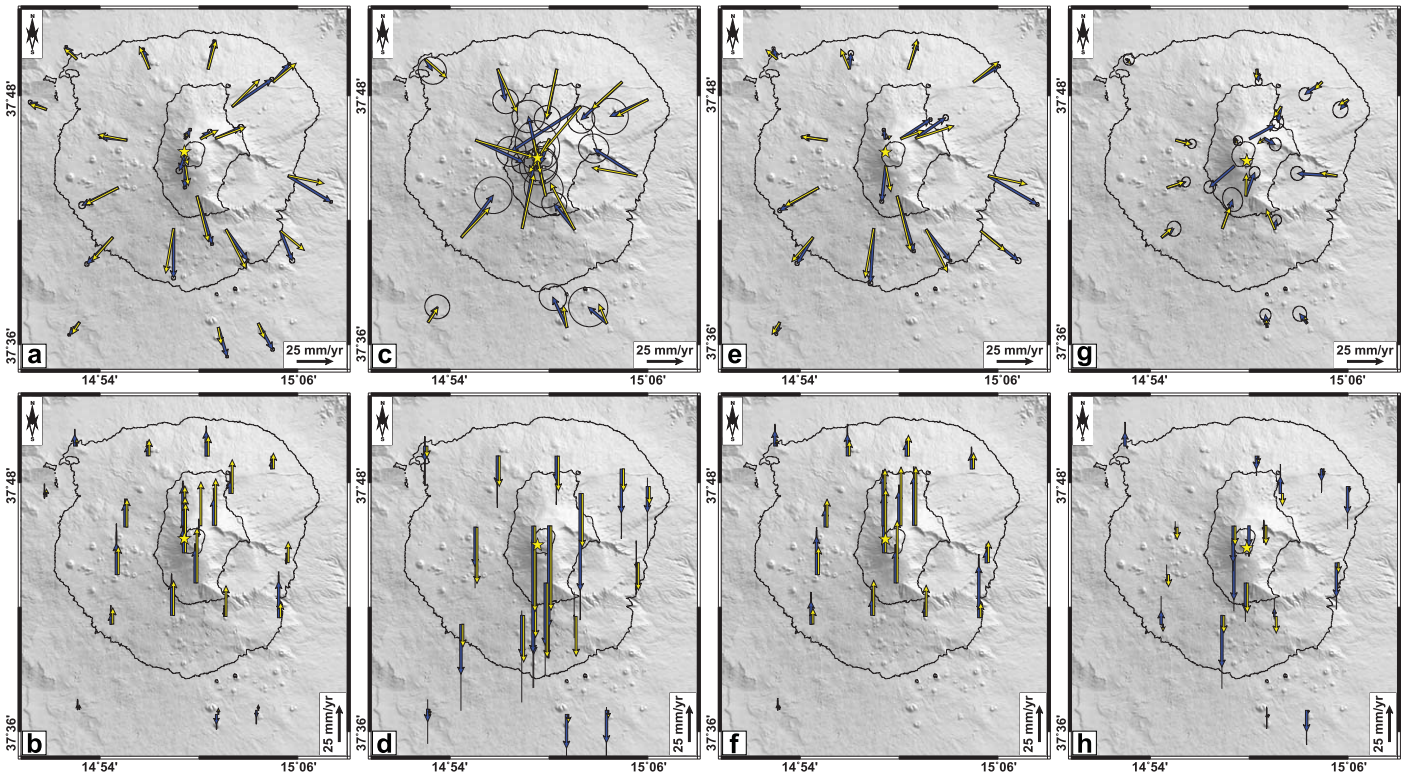

Figure 3. Comparison between observed (blue arrows) and (a, c, e, g) modeled (yellow arrows) horizontal and (b, d, f, h) vertical deformation fields relevant to the considered time intervals: (a, b) for T1 (1 July 2015 to 2 December 2015), (c, d) for T2 (2 December 2015 to 9 December 2015), (e, f) for T3 (9 December 2015 to 17 May 2016), and (g, h) for T4 (17 May 2016 to 20 May 2016). The surface projections of modeled sources are reported as yellow stars (see Table 1 for details).

Table 1
Parameters[a] *of the Modeled Sources Inferred for Intervals Analyzed in This Study*

Parameters	T1	T2	T3	T4
Easting (m)	498,829 ± 273	499,098 ± 328	498,915 ± 158	499,903 ± 640
Northing (m)	417,8627 ± 251	417,8083 ± 273	417,8595 ± 193	417,7831 ± 446
Depth (m bsl)	5,661 ± 471	5,273 ± 634	5,028 ± 459	4,910 ± 637
a axis (m)	923 ± 136	711 ± 172	1,142 ± 110	988 ± 190
a/*b* ratio	0.29 ± 0.08	0.68 ± 0.12	0.19 ± 0.10	0.33 ± 0.13
Azimuth (°)	216.1 ± 15.2	1.5 ± 17.5	222.7 ± 16.6	183.9 ± 32.3
Dip (°)	72.0 ± 9.2	86.4 ± 10.6	64.7 ± 13.5	67.8 ± 16.6
ΔP (Pa)	$9.42 \pm 0.31 \times 10^8$	$-2.13 \pm 0.42 \times 10^8$	$8.18 \pm 0.29 \times 10^8$	$-1.78 \pm 0.48 \times 10^8$
ΔV (10^6 m^3)	6.48	−3.73	4.55	−1.96

[a] *a* and *b* are the lengths of the major and the minor axes of the spheroidal pressure source (Yang et al., 1988), respectively. ΔV is calculated as $\Delta V = \Delta P a b 2\pi/\mu$ according to Tiampo et al. (2000), where ΔP is the exceeding pressure and μ is the rigidity modulus of the elastic half-space. For each parameter, errors (at 95% of confidence) were estimated by adopting a Jackknife-sampling method (Efron, 1982). Coordinates are in UTM33N projection.

local reference frame to isolate the volcanic deformation from the background tectonic pattern (see Palano et al., 2010 for details). T1 and T3 show a general outward radial pattern, indicating a pressurization of the plumbing system (Figures 3a, 3b, 3e, and 3f); conversely, T2 is characterized by a general contraction of the volcano edifice, indicating a depressurization of the plumbing system (Figures 3c and 3d). As mentioned above, T4 is characterized by a complex pattern (Figures 3g and 3h): overall it is characterized by a general contraction of the volcano edifice, however the ground deformation pattern of a few stations close to the summit area (ECPN and ECNE) reflect a fragile response to the opening of the shallow fracture field during the lava fountaining episodes.

The surface deformation for each detected stage (e.g., both horizontal and vertical GPS velocities along with associated uncertainties) was used to constrain isotropic half-space elastic inversion models. The inversions were performed using the genetic algorithm approach (e.g., Tiampo et al., 2000) and adopting the Yang et al. (1988) analytical model. We also adopted the method of Williams and Wadge (2000) in order to include topography.

For T1 (Figures 3a and 3b), the modeled source is located beneath the western side of summit area at a depth of ~5.7 km bsl. It is given by a near vertical prolate spheroid and is characterized by a positive volume change of 6.48×10^6 m^3 (Table 1). For T2 (Figures 3c and 3d), the best model is given by a vertically elongated spheroid source centered at ~5.3 km (bsl) beneath the south-western side of summit area. It is characterized by a negative volume change of 3.73×10^6 m^3 (Table 1). For T3 (Figures 3c and 3d), the modeled source is located beneath the western side of summit area at a depth of ~5.0 km bsl. It is given by a near vertical prolate spheroid and is characterized by a positive volume change of 4.55×10^6 m^3 (Table 1). The best model for T4 is given by a source located at a depth of ~4.8 km bsl beneath the SEC and characterized by a negative volume change of 1.96×10^6 m^3 (Table 1). During this last computation, we excluded the ground deformation pattern measured at ECPN and ECNE stations since their motion is mainly related to the opening of the shallow fracture field crossing the summit area (see supporting information Figure S1).

Overall, the final results show a reasonable fit between modeled and observed deformation fields (Figure 3). Some mismatches in both 3-D direction and magnitude between the modeled and observed geodetic velocities can be seen: these are possibly linked both to the simplified assumption of our model (i.e., homogeneous, isotropic, and elastic half-space) or to local effects (monument instability and/or motion along nearby active fractures/faults).

3.2. Seismic and Infrasonic Data

Volcanotectonic (VT) earthquakes, generally associated with rock shear failure due to several phenomena such as magma intrusion, withdrawal, cooling, and regional tectonic forces (e.g., McNutt, 2005), take place at Mt. Etna and affect the entire volcano edifice from the summit area down to ~30 km bsl (e.g., Patanè et al., 2013). In order to follow the evolution in time of the VT activity during June 2015 to August 2016, the

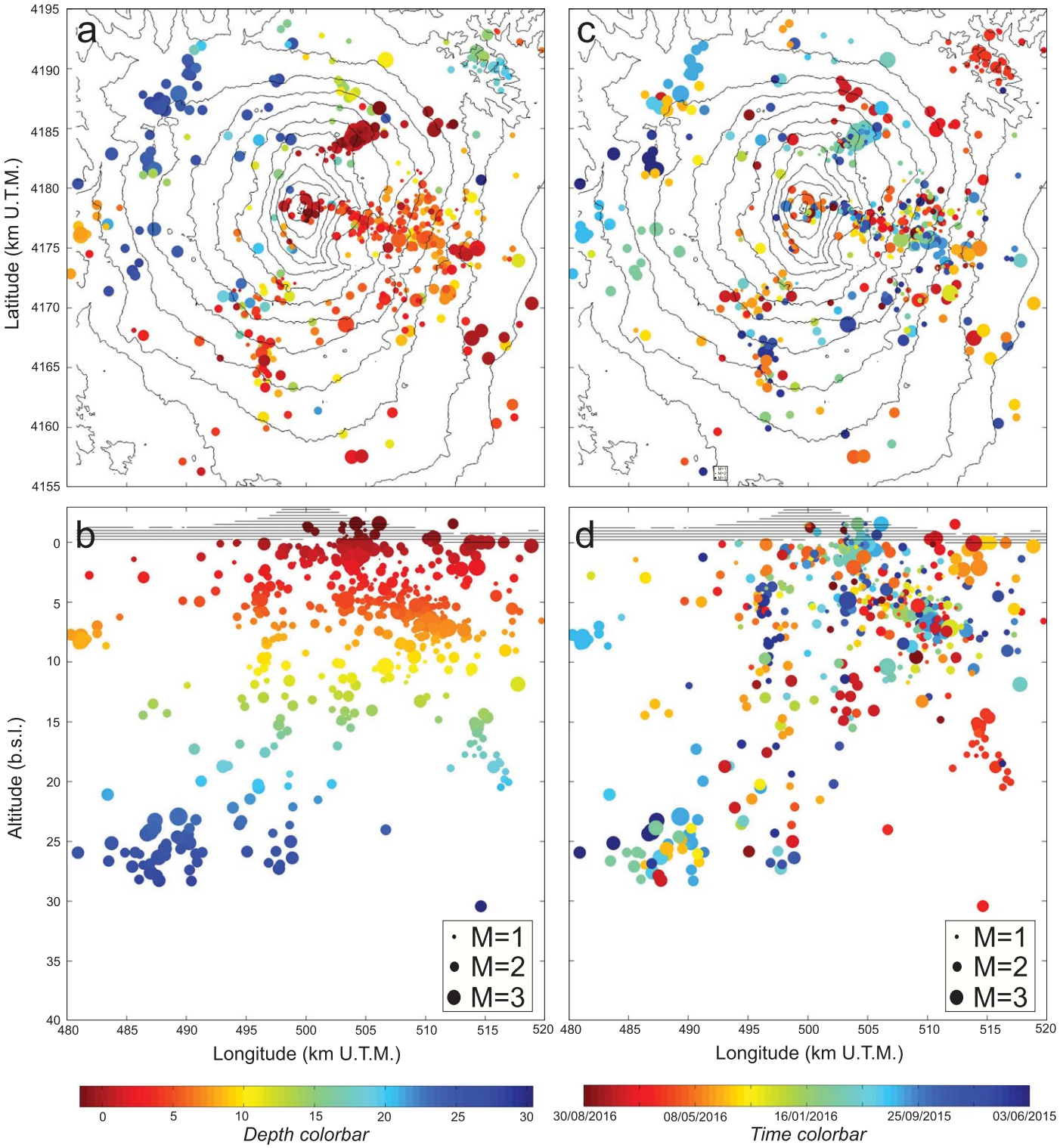

Figure 4. (a, c) Maps and (b, d) sections of Mt. Etna showing the locations of the VT earthquakes taking place during 1 June 2015 to 31 August 2016 at Mt. Etna. In Figures 4a and 4b, the colors of the dots indicate the VT focal depth, in Figures 4c and 4d, the colors indicate their occurrence time. The size of the dots is proportional to the earthquake magnitude (see legend in the bottom right corners of the sections).

daily number of VT earthquakes and the corresponding cumulative strain release are reported in Figure 2g, and their depth over time is shown in Figure 2h. In addition, in Figure 4, a map showing the VT locations during the period of interest is reported (http://www.ct.ingv.it/ufs/analisti/catalogolist.php; Gruppo Analisi Dati Sismici, 2017).

At Mt. Etna, studies on volcanic tremor and long period (LP) events have provided useful information for both monitoring and research purposes. In particular, these seismovolcanic signals and their variations over time have turned out to be strictly related to eruptive activity (e.g., Patanè et al., 2008; Viccaro et al., 2014), as well as having recently been used to highlight pressurization and depressurization phenomena within the plumbing system (Cannata et al., 2015). In addition, decade-long observations at Mt. Etna show that LP events and volcanic tremor are generally not colocated and often show different temporal patterns (e.g., Cannata et al., 2015). This could suggest that they do not share the same source. The seismovolcanic signals are investigated by the seismic data recorded by the permanent seismic network run by INGV, Osservatorio Etneo - Sezione di Catania. In particular, 17 stations, equipped with broadband three-component Trillium 40s seismometers (Nanometrics™) and recording at a sampling rate of 100 Hz, are routinely used for volcanic tremor and LP events study (Figure 1a).

Concerning volcanic tremor, we investigated its temporal variations of amplitude and source locations. In order to track the amplitude changes through time, we calculated the root-mean-square (RMS) of the seismic signal recorded by the vertical component of ESLN seismic station (Figure 1a) within 10 min-long sliding windows and filtered in the band 0.5–5.5 Hz (Figure 2c). To locate the volcanic tremor centroid, we applied a grid-search method based on spatial-seismic-amplitude distribution, assuming propagation of body waves in a homogeneous medium (Cannata et al., 2013; Di Grazia et al., 2006; Figures 2d and 5). In the location case, the investigated frequency band was 0.5–2.5 Hz, routinely analyzed to highlight the main migrations of the tremor centroid (Cannata et al., 2013; Patanè et al., 2008). The average location errors, calculated by the jackknife method (Cannata et al., 2013; Di Grazia et al., 2006), were equal to $\sim$0.4, $\sim$0.5, and $\sim$0.8 km for longitude, latitude, and altitude, respectively, consistent with those estimated in previous works (e.g., Patanè et al., 2008; Viccaro et al., 2016a).

As for LP events, the variations in time of daily occurrence rate, as well as the changes in amplitude at ECPN station (Figure 1), were investigated (Figure 2e). ECPN station is routinely used as the reference station for LP events study at Etna (Cannata et al., 2009, 2015). Concerning the amplitude, we calculated and plotted the time series of the daily 25°, 50°, and 75° percentile calculated on the event peak-to-peak amplitudes (Figure 2e, right axis). Indeed, these time series, less affected by outliers than average and standard deviation, allow following the evolution over time of LP event amplitudes.

Volcanic infrasonic signal at Mt. Etna is generally made up of infrasonic events characterized by durations of less than 1 to over 30 s, impulsive compression onsets, and peaked spectra with most of the energy in the frequency range 0.3–6.0 Hz (Cannata et al., 2013). These events can be investigated through the infrasonic permanent network, run by INGV, Osservatorio Etneo - Sezione di Catania. Such a network is composed of 10 stations equipped with GRASS 40AN microphones with a flat response at a sensitivity of 50 mV/Pa in the frequency range of 0.3–20,000 Hz (Figure 1). The infrasonic signals are acquired at a sampling rate of 50 Hz.

The infrasound event sources are located by a grid-search technique based on the brightness function (e.g., Cannata et al., 2013; Kao & Shan, 2004). In Figure 2f, a stacked histogram showing the daily number of infrasonic events located in NSEC, NEC, and VOR/BN areas is shown. The locations are also shown in the map in Figure 5a. The variability in the number of located events does depend not only on the level of infrasonic activity of each crater but also on the number of infrasonic stations properly working. In particular, from the end of November 2015, the number of infrasonic stations dropped from 9–10 to 6–8.

On the basis of the main temporal variations of the seismovolcanic and infrasonic signals, we can distinguish the following intervals (Figure 2). From July to end of November 2015 (roughly corresponding with period T1), a gradual increase of the amplitude of volcanic tremor, whose source was located shallow below NSEC, can be observed. Also the VT activity shows an intensification from October involving both deep and shallow seismicity. In addition, the time series of the daily 25°, 50°, and 75° percentile of the LP event amplitude also showed an increasing pattern reaching the highest values of the investigated period during September–October. Noteworthy, a sharp decrease of LP amplitude was observed on 1 November 2015 at the same time as a very energetic LP event that was also accompanied by a change in pattern of volcanic

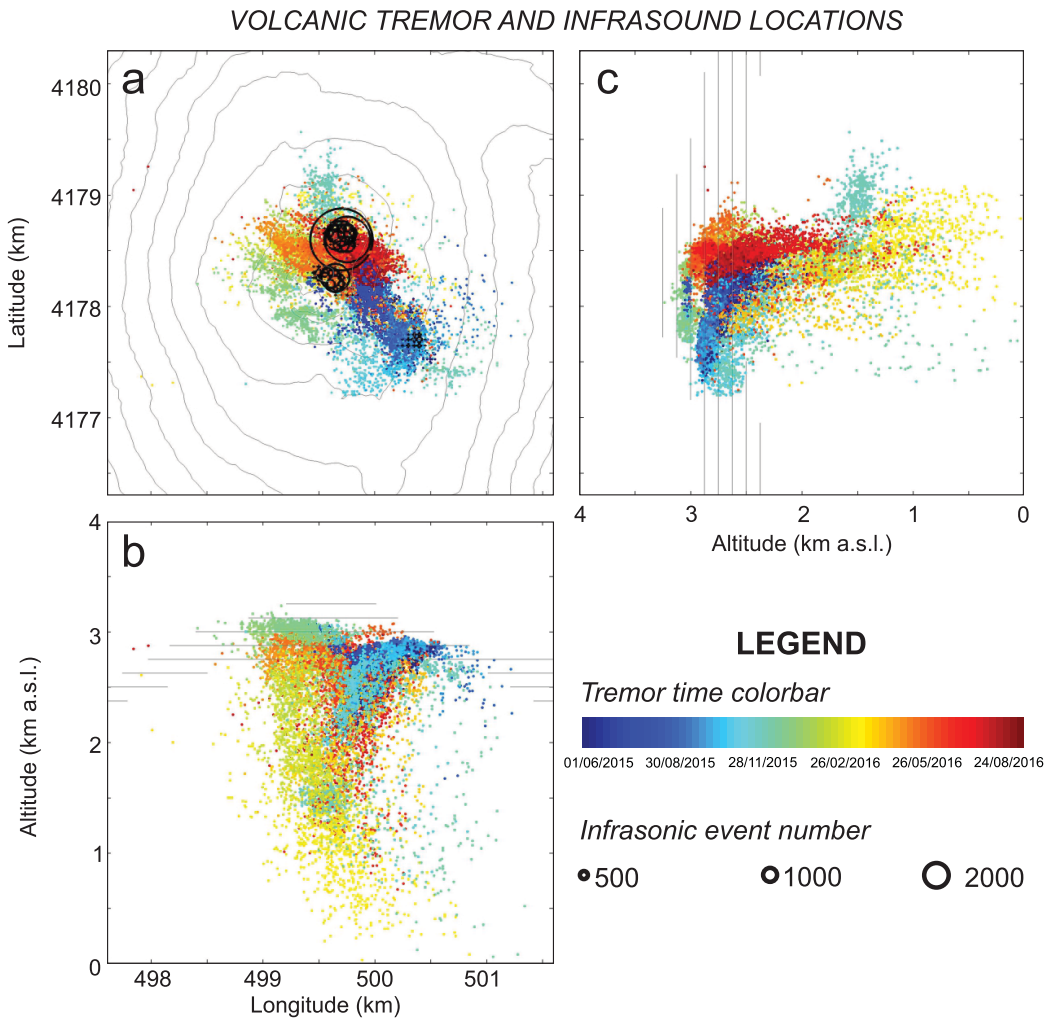

Figure 5. (a) Map and (b, c) sections of Mt. Etna with locations of the volcanic tremor centroids (color dots) and infrasonic events (black circles in "a") during June 2015 to August 2016. The color of the dots relates to different times (see legend in the bottom right corner and Figure 2d). The radii of the black circles in "a" are proportional to the number of locations of infrasonic events in each grid node (see legend in the bottom right corner).

tremor RMS (see also supporting information Figure S2). The main infrasound source during June–November 2015 was NEC.

From the end of November to mid-December 2015 (T2), corresponding with the eruptive activity at VOR, NSEC, and NEC craters, we observed sharp increases in volcanic tremor amplitude, deepening of its source centroid and intensification of NSEC and VOR infrasonic activities. From 7 to 10 December 2015, the most energetic VT swarm of the period of interest took place at depth 0–3 km bsl beneath the north-eastern volcano flank. At the end of the eruptive period, the amplitude of volcanic tremor sharply decreased down to values comparable to the ones observed at the beginning of the investigated interval (Figure 2c).

Successively, from mid-December 2015 to the onset of May 2016 (T3), the amplitude of volcanic tremor exhibited a gradually increasing trend, culminating again with the eruptive activity of mid-May. The volcanic tremor source centroid, whose epicenter shifted northwestward from NSEC to the area of VOR, BN, and NEC, deepened during mid-January to the onset of April 2016, with maximum depth of ~1 km asl. Unlike volcanic tremor, time series of the daily 25°, 50°, and 75° percentiles of the LP event amplitude showed very low values, suggesting low LP activity. VT earthquakes showed a slight intensification from April to mid-May 2016. Similar to the VT increase observed in October–December 2015, also in this case the earthquakes were spread over a large focal depth range. The almost complete lack of infrasonic locations during this

interval cannot be simply due to the decrease in the number of properly working stations. Indeed, the infrasonic activity reappears again during May and July–August 2016, not accompanied by any meaningful change in network effectiveness. Hence, it can be inferred that T3 interval was characterized by very low infrasonic activity.

The period May 2016 (including T4), characterized by eruptive activity at VOR, NSEC, and NEC craters, showed high tremor amplitudes, shallow tremor source centroids, and a resumption of infrasonic activity from NSEC, VOR, and NEC. Such a period has similar patterns to the other paroxysmal period T2.

Finally, June 2016 (T5) is similar to T3 period from the seismovolcanic and infrasonic point of view: low amplitude volcanic tremor, deepening of tremor source centroid, low LP event amplitudes, and an almost complete lack of infrasonic locations.

4. Petrological Characteristics of the Erupted Products

4.1. Sampling and Analytical Methods

Rheomorphic lava and air-quenched tephra samples were taken in the summit area at the end of each paroxysmal eruption that occurred at VOR crater. Seven samples refer to the December 2015 activity, whereas eight are from the May 2016 eruptions. Major element compositions for all the collected samples were analyzed at the Dipartimento di Scienze Biologiche, Geologiche e Ambientali (University of Catania, Italy) by means of a Philips PW2404 WD-XRF on powder pellets correcting the matrix effects. Loss on ignition was determined by gravimetric methods. Trace element abundances were measured at the SGS Laboratories of Toronto (Ontario, Canada). Powdered rock samples were fused by Na-peroxide in graphite crucibles and dissolved using dilute HNO_3. Trace element analyses were then obtained by means of a Perkin Elmer ELAN 6100 inductively coupled plasma mass spectrometer. Four calibration runs were performed on international certified reference materials at the beginning and end of each batch of five samples. Precision is better than 5% for all the trace elements analyzed, and accuracy is on the same order of magnitude. The complete major and trace element data set for the analyzed samples is available as supporting information Table S1.

Forty-five plagioclase and forty-one olivine crystals, representative of crystal textural variability, were selected for petrological analyses. We measured An% and FeO wt % composition along core-to-rim profiles of the plagioclase crystals for each textural type, and Fo% variations along rim-to-rim transects for olivine crystals. Spacing between individual analysis spots in all crystals ranges between 5 and 10 μm depending on crystal sizes. High-resolution back-scattered electron images (BSE, 1,024 × 864 pixels) and microanalytical data on plagioclase and olivine were obtained on polished thin sections at the Dipartimento di Scienze Biologiche, Geologiche e Ambientali, University of Catania (Italy) using a Tescan Vega-LMU scanning electron microscope (SEM) equipped with an EDAX Neptune XM4–60 microanalyzer operating by energy dispersive system (EDS) characterized by an ultra-thin Be window coupled with an EDAX WDS LEXS (wavelength dispersive low-energy X-ray spectrometer) calibrated for light elements. Operating conditions were set at 20 kV accelerating voltage to obtain high-contrast BSE images and the analysis of major element abundances in mineral phases. Repeated analyses on internationally certified An-rich plagioclase, Fo-rich olivine, and glass inner standards during the analytical runs ensure precision for all the collected elements in the order of 3–5%. Accuracy is on the order of 5%. The complete data set for the analyzed plagioclase and olivine crystals is available in the supporting information Tables S2 and S3.

4.2. Petrographic and Geochemical Features of the Volcanic Rocks

Volcanic rocks erupted during the activity of December 2015 and May 2016 at VOR crater are K-trachybasalts with major and trace element compositions consistent with those of the products erupted at NSEC during the 2011–2013 paroxysmal eruptions (supporting information Table S1; Viccaro et al., 2015). It is worth noting that no significant compositional differences have been observed between products emitted during the December 2015 and May 2016 eruptions (supporting information Table S1). They have porphyritic textures (Porphyritic Index from 15% to 25%) and are highly vesiculated (40–60% vesicles). All the lava samples are characterized by vitrophyric to hyalopilitic groundmass with the only exception of lavas erupted during the first episodes of May 2016, which have prevalent intersertal textures. We also observed the presence of sideromelane in tephra erupted during the episode of 3 December 2015. Among phenocrysts, plagioclase constitutes the dominant mineral phase (50–60%), followed by clinopyroxene (25–30%),

olivine (10–15%), and opaque oxides (<5%). The same mineral phases, in similar proportions, have been also observed as microphenocrysts (<100 μm diameter).

Textural and compositional characteristics of the observed mineral phases resemble those of crystals previously emitted during the 2011–2013 activity at NSEC. In particular, crystals of plagioclase and olivine show a wide range of compositions, textures, and sizes. Plagioclase mainly occurs as single large crystals (up to 4 mm diameter) with euhedral to anhedral habitus and composition from andesine (An_{46}) to anorthite (An_{90}). Olivine is mainly present as crystals of size <1.5 mm, and composition from Fo_{69} to Fo_{89}. Both plagioclase and olivine crystals are characterized by a variety of textures and zoning patterns that are described in detail in the following sections. Clinopyroxene is augitic or diopsidic in composition and occurs as single crystals or aggregated with other phases. The microphenocrysts (100–200 μm) are generally subhedral, whereas the euhedral habitus is common in crystals with size >1 mm. Some crystals are affected by disequilibrium and show spongy-textured rims, a feature particularly evident in clinopyroxene crystals from eruptions of May 2016. Opaque oxides are constituted by subhedral to anhedral crystals of titaniferous magnetite. They are frequently enclosed in olivine and clinopyroxene, a feature that testifies to their early nucleation and growth.

4.3. Textural and Compositional Features of Plagioclase Crystals

Plagioclase crystals have complex textures, resulting from the combination of growth and disequilibrium textures at the core and rims. Following the nomenclature introduced by Viccaro et al. (2010) for the dominant plagioclase textures found in historic and recent products of Mt. Etna, we observed at least five main textural types, which are described below by taking into account the anorthite zoning (mol %) together with variations of FeO (wt %). The textural types are the following: (a) oscillatory zoning (Type 1); (b) pervasive dissolution/resorption textures (Type 2); (c) coarse-sieve textures at the plagioclase core (Type 4); (d) sieve textures at the crystal rim (Type 5). In some cases, we observed the presence of patchy textures (Type 3) at the core of large (>1,000 mm) phenocrysts, and of swallow-tailed textures in microphenocrysts.

Wholly oscillatory-zoned crystals (~10% of the total textures, Figures 6a and 7a) are mainly small (<500 μm) and medium-sized crystals (500–1,000 μm) with core composition between An_{50} and An_{65}. Only few crystals in tephra erupted during the episode of 3 December 2015 have a more calcic core composition at $\sim An_{80-85}$. Small-scale anorthite oscillations characterize the core of these crystals, with amplitude of $\sim\Delta An_5$ or less, and wavelength <10 mm. The plagioclase rim shows larger An oscillations with $\sim\Delta An_{5-10}$ amplitude and 20–30 mm wavelength. The FeO content ranges between 0.6 and 1.0 wt % in all the investigated crystals and generally varies in accordance with An at the crystal interior, but it becomes increasingly discordant toward the rim.

Among the disequilibrium textures, we observed at the plagioclase core, the Type 2 (strongly dissolution/resorption, Figure 6b and 7b) is the most abundant, mainly for what concerns the products of December 2015, where Type 2 constitutes the 40–50% of the total textures in phenocrysts. Contrariwise, coarsely sieved textures (Type 4, Figures 6c and 7c) are common at the core of crystals emitted during the first paroxysmal eruption of May 2016 (~40%). In correspondence of both Type 2 and 4 textures, the An content is generally higher than An_{80}, reaching An_{90} in some crystals found in products erupted in May 2016. FeO ranges from 0.6 to 1.0 wt % and forms concordant trend with the An zoning. In the crystal zone surrounding the core, the An composition decreases until An_{50-60}.

Type 5 crystals (sieve textures at the rim) are ~30–40% of the total analyzed plagioclase phenocrysts in products emitted at VOR between 2015 and 2016. This type of texture is commonly characterized by increase of the An (maximum ΔAn ~20) and FeO (maximum ΔFeO ~0.4 wt %) contents with respect to the surrounding plagioclase zones (Figures 6c, 7c, and 7d). However, crystals from the eruption of 3 December 2015 display an increase of FeO not accompanied by concomitant An increase, which is rather constant (Figure 6d).

4.4. Compositional Zoning of Olivine Crystals

Olivine crystals generally have euhedral habitus at the small and medium size (<1 mm), whereas the larger crystals (with size up to 1.5 mm) are commonly resorbed and their edges are usually characterized by embayments. Disequilibrium textures occur with a frequency of 10–20% in all the analyzed samples.

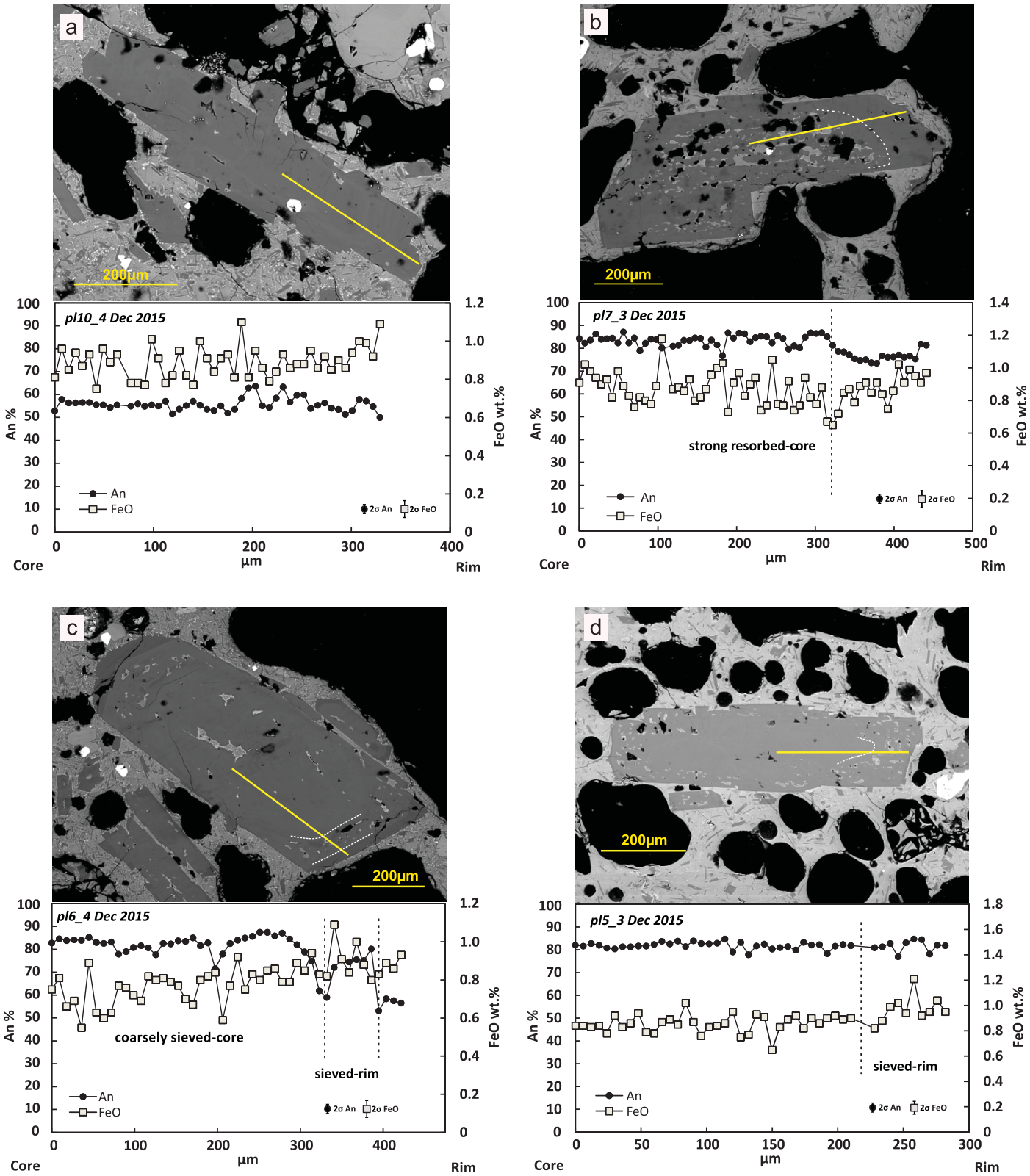

Figure 6. Core-to-rim profile for An mol% (black circles) and FeO wt % (white squares) and associated textures in plagioclase crystals found in the volcanic products emitted by VOR crater during December 2015. Yellow lines in the BSE images indicate the direction of the SEM-EDS/WDS compositional traverses.

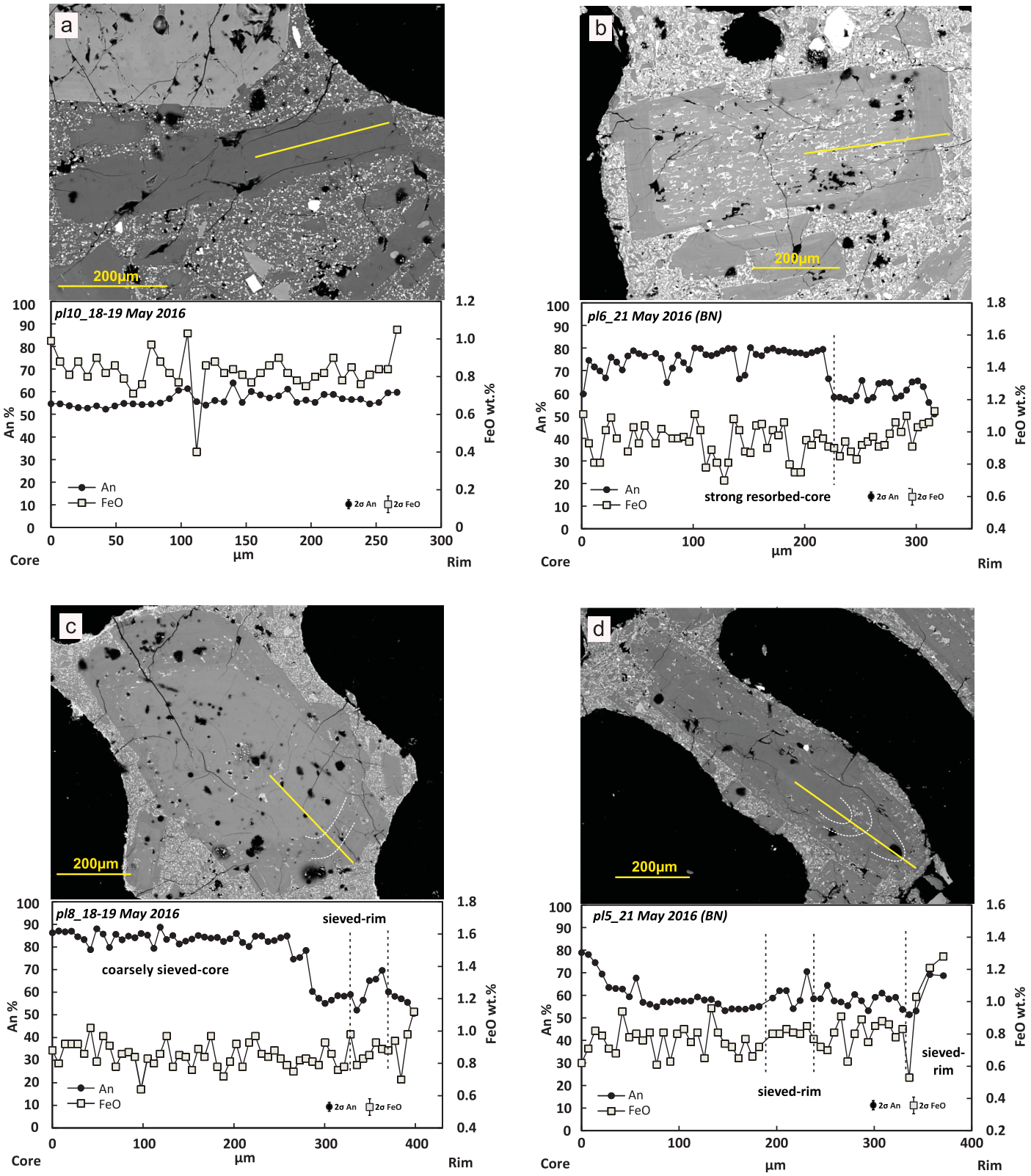

Figure 7. Core-to-rim profile for An mol% (black circles) and FeO wt % (white squares) and associated textures in plagioclase crystals found in the volcanic products emitted by VOR crater during May 2016. Yellow lines in the BSE images indicate the direction of the SEM-EDS/WDS compositional traverses.

The composition of olivine crystals is rather homogeneous at the core, whereas rims are typified by complex zoning patterns with normal zoning shifting to reverse or vice versa (Figure 8). Based on the core composition, we have grouped crystals into five olivine populations (OP):

OP1 ($Fo_{83–84}$) represents ~10% of the total analyzed crystals. They are typically normally zoned crystals with rim composition ranging from Fo_{74} to Fo_{75} (Figure 8a). Sometimes the normal zoning pattern surrounding the core is followed by a reverse zoning toward the crystal edge, where the Fo concentration increases up to Fo_{85}. We also observed one single crystal from the eruption of December 2015 with reversely zoned interior, characterized by a ~Fo_{83} core composition that becomes slightly more forsteritic toward the rim (~Fo_{84}), and then decreases to Fo_{80} at the outermost rim (Figure 8b).

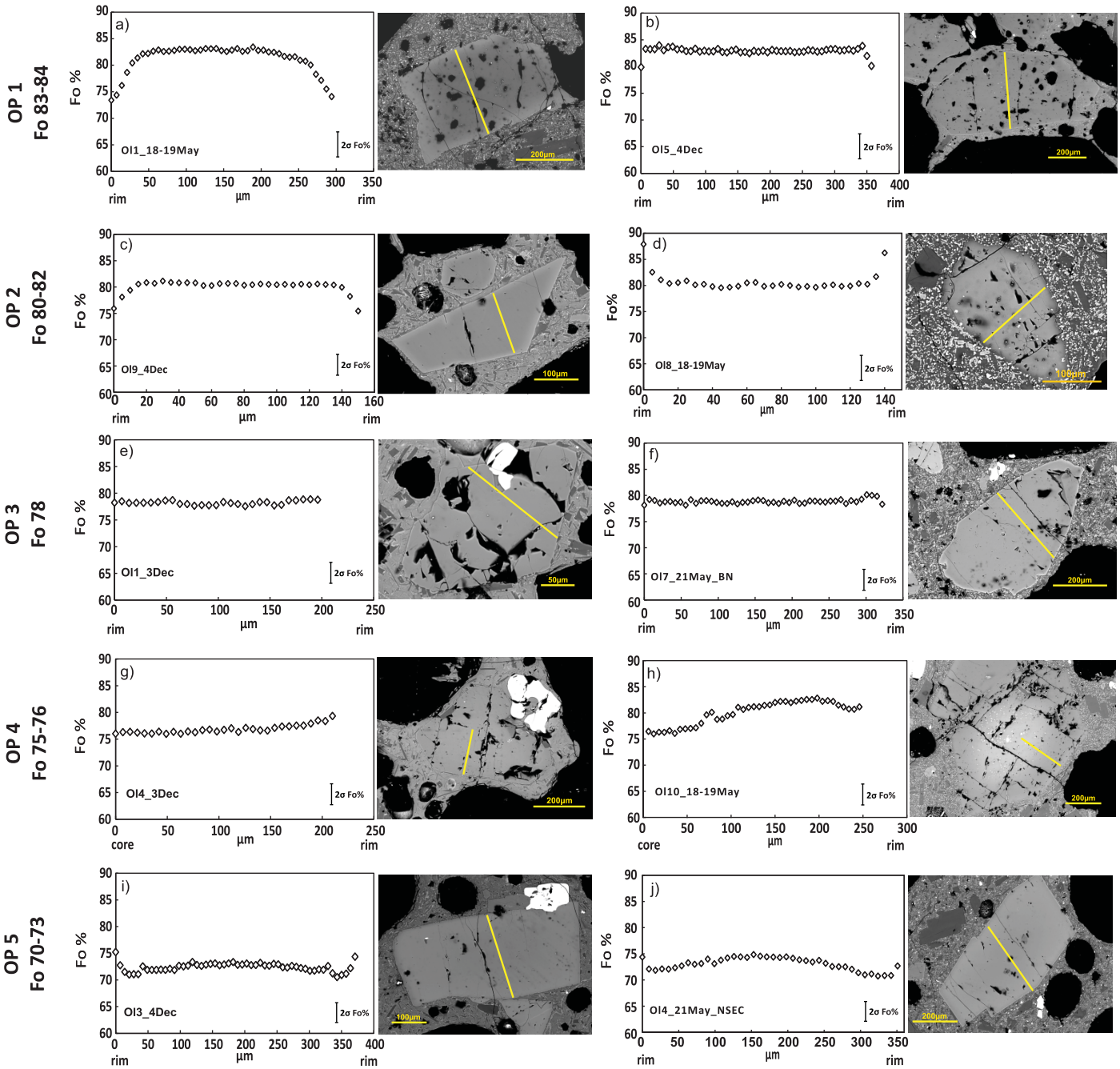

Figure 8. Variation of Fo mol% in olivine crystals of the distinct populations (OP) recognized in products erupted during December 2015 and May 2016. Yellow lines in the BSE images indicate the direction of the SEM-EDS/WDS compositional traverses.

OP2 (Fo_{80-82}), constituting ~29% of all the observed olivine crystals, are particularly present in tephra erupted during the episode of 4 December 2015, as well as in lavas that overflowed from the west part of BN on May 2016. The majority of OP2 crystals have rims with normal zoning, which generally record a decrease in Fo concentration to Fo_{75} (Figure 8c). We also noted the presence of few crystals from the first eruptive phase of May 2016 that show reversely zoned rims, which are highly forsteritic (Fo_{85-89}), and are often affected by disequilibrium textures similar to sieve textures (Figure 8d).

OP3 (Fo_{78} core composition) includes only three olivine crystals that are representative of the eruptions of 3 December 2015 and 21 May 2016 samples. All these crystals have rather homogeneous core composition at Fo_{78} and a slight reverse zoning at the rim (Fo_{79-80}, Figures 8e and 8f).

OP4 (Fo_{75-76}) crystals constitute ~17% of the total olivine crystals and are dominant in tephra rocks erupted during December 2015. The rims of these crystals display either normal zoning (decreasing concentration to Fo_{73-74}), mainly characterizing products of 4 December 2015, or reverse zoning patterns (increasing concentration to Fo_{79-80}), more abundant within the eruptive products of 3 December 2015 (Figure 8g). A single crystal found in lava rocks erupted during May 2016 displays a more complex zoning pattern with destabilized cores marked by spongy textures (Figure 8h).

OP5 (Fo_{70-73}) crystals are common in all the samples under investigation, and occur with high frequency (~37%). Typically, these crystals have low-Fo cores (Fo_{70-73}) mantled by a reversely zoned region at higher Fo composition (Fo_{75-78}). However, OP5 olivines may also show more complex zoning patterns, with normal zoning at the rim, then changing to reverse toward the edge (up to Fo_{75}, Figures 8i and 8j).

Olivine populations and associated zoning patterns described in this work are comparable with those recognized in products previously emitted at the NSEC crater during the period 2011–2013 (Giuffrida & Viccaro, 2017). However, among crystals emitted at VOR crater we identified a new zoning type that has homogeneous Fo_{80-82} cores and reverse-zoned rims with Fo contents up to Fo_{89}. This new type of zoning is exclusive of products erupted during the early phase of activity of May 2016 (i.e., eruptions of 18–19 May 2016).

5. Discussion

5.1. Geophysical Constraints on Magma Dynamics

The integration of ground deformation, seismic, and infrasonic data allows reconstructing the magma dynamics within the plumbing system from a few km bsl up to the shallowest portions, corresponding with the summit craters.

In particular, ground deformation data provided useful constraints on the magma movement along those portions of the plumbing system located at intermediate depths. More in detail, the modeling of ground deformation data inferred the presence of magmatic sources beneath the summit area in the 4.9–5.7 km bsl depth interval. Within the estimated uncertainties, the positions of all the modeled sources spatially overlap and, therefore, they can reasonably be considered as a unique magmatic reservoir. Moreover, this reservoir would correspond to depth level where magma densities and surrounding host rock densities are balanced, favoring magma storage. In addition, it can be considered as a permanent zone of magma storage at Mt. Etna given its recurrent activity over the last decade (e.g., Gambino et al., 2016; Palano et al., 2017; Spampinato et al., 2015; Viccaro et al., 2016a). On the other hand, volcanic tremor and LP events allow highlighting shallower magma migrations, as well as pressurization/depressurization phenomena affecting the upper parts of the plumbing system (generally above the sea level; e.g., Cannata et al., 2015). During the investigated time interval, the sources of volcanic tremor were located below the summit craters at depth ranging from ~1 to 3 km asl. Most of the shallowest centroid locations (~3 km asl) fall within VOR/BN and NSEC areas and are associated with degassing and eruptive activities of these craters. The deeper locations (down to 1 km asl) are likely to be related to magma migration in this portion of plumbing system, where a shallow magma storage was inferred at 1–2 km asl by Patanè et al. (2013) and Gambino et al. (2016). Infrasonic data provide insights into the shallowest portions of the plumbing system, corresponding with the degassing/eruptive vents, and their variations over time. The infrasonic sources active during the period of interest were NSEC, NEC, and VOR craters. In particular, the infrasound emission from NSEC accompanied only Strombolian activity and lava fountains, while infrasonic activity of NEC and VOR was associated with both explosive eruptions and simple degassing. NEC has emitted infrasound during simple

degassing at least since the deployment of the first permanent infrasonic station at Mt. Etna in 2006 (e.g., Spina et al., 2015), and VOR since September 2013 (Cannata et al., 2015). Finally, the VT earthquake hypocenters are spread over the entire volcano edifice and, due to the large variety of their causative processes (e.g., McNutt et al., 2015), do not necessarily correspond with portions of the plumbing system. In particular, the eastern flank is dominated by shallow VT seismicity partially following NNW-SSE trending extensional seismogenic structures (e.g., Mattia et al., 2015), while the western flank shows deeper seismicity.

Focusing on the time interval analyzed in this work, the magmatic reservoir, located beneath the western side of summit area at a depth of ~5.7 km bsl, pressurized from June 2015 (T1), as suggested by the inflation pattern of the ground deformation data. During the same time interval (July to end of November 2015), gradual but clear increases in amplitude of both volcanic tremor and LP events were observed. Such evidences were interpreted at Mt. Etna (e.g., Cannata et al., 2015), as well as at other volcanoes (i.e., Mount St. Helens, Moran et al., 2008; Colima, Varley et al., 2010), as resulting from pressurization of the shallow portions of the plumbing system. The energetic LP event recorded on 1 November 2015 was time related to changes in the patterns of both LP amplitude and volcanic tremor RMS amplitudes. A similar phenomenon was observed on 5 September 2013, when a strong LP event (with peak-to-peak amplitude of 0.003 m/s at 1 km from the source) accompanied the expulsion of a plug at BN, producing decrease in amplitude of LP events and volcanic tremor. This episode was interpreted as the end of the pressurization of the shallow plumbing system, which gave rise to the gradual resumption of activity at NSEC (Cannata et al., 2015). Also in the November 2015 case, the energetic LP event could be associated with a plug expulsion at one of the summit craters and took place during a period of resumption of explosive activity at the summit craters. In addition, also an intensification of the VT activity took place from October, involving almost the whole volcano edifice. Such an increase can be due to the aforementioned pressurization phenomena affecting even the deeper portion of the plumbing system, as testified by the occurrence of seismicity down to 25 km bsl.

These phenomena led to the eruptive activities at the beginning of December 2015, which involved three of the summit craters VOR, NSEC, and NEC craters, as also suggested by the three active infrasonic sources. Such eruptive activities (T2) generated a fast and vigorous depressurization of the reservoir located in the 4.9–5.7 km bsl depth range, as well as of the shallower portions of the plumbing system (1–3 km asl), testified by further decreases in both volcanic tremor and LP events amplitude (beginning of T3). This time, the pressurization of the deep reservoir (T3) was likely accompanied by pressurization of the shallower portions of the plumbing system, as testified by the gradual increase of volcanic tremor amplitude. However, in this case we did not observe an increase in LP amplitudes. Such phenomena led again to the volcanic activity occurring during mid-May 2016, with the onset of a shallow fracture field extending from the NEC up to the SEC, crossing the whole summit area, and to depressurization in T4 as a consequence of the magma withdrawal.

5.2. Thermodynamic and Kinetics Constraints of the Magma Storage and Transfer

A combination of growth and resorption features of plagioclase crystals observed in products from the 2015–2016 activity reflect changing chemical/physical conditions of the magmatic system during their histories from nucleation to eruption. For instance, the development of oscillatory-zoned patterns in plagioclase requires crystallization conditions that are close to equilibrium (Allegre et al., 1981). This means that wholly oscillatory-zoned plagioclases form in magmatic environments characterized by very limited *P*, *T*, and volatile component variations. Significant changes of the thermodynamic parameters of the plagioclase host melt may severely affect the plagioclase stability field, enhancing processes of dissolution/resorption that are usually associated with prominent compositional changes.

Type 2 and 4 textures commonly affect the cores of plagioclase crystals found in lavas and tephra erupted during the whole investigated period. The mechanisms responsible for such features are attributed to processes of crystal destabilization during magma decompression at different rates and/or volatile composition (cf., Giuffrida & Viccaro, 2017; Viccaro et al., 2016b). Plagioclase stability may be reduced during magma ascent due to the increase in the partial volatile pressure of a magmatic system ascending under water undersaturated conditions (Nelson & Montana, 1992) or, in the case of $H_2O + CO_2$-bearing magmas, under volatile-saturated conditions since the most of water remains dissolved in the melt until very low pressure conditions (<200 MPa; Giuffrida & Viccaro, 2017). Such processes could also be responsible for changing the plagioclase composition that becomes more calcic (Blundy & Cashman, 2008). Highly pervasive

resorption textures (Type 2) at high An concentration (>An_{80} mol %) preferentially characterize plagioclase crystals emitted during the eruption of 3 December 2015. This may indicate that prior to this paroxysm, magmas rose up to the surface at higher ascent velocity and/or higher water concentration than magmas feeding the following eruptions at VOR crater, therefore allowing a higher degree of destabilization in plagioclase of the 3 December 2015 eruption.

Correlation of An and FeO zoning in correspondence to the dusty sieve textures (Type 5) allows us to distinguish between the different mechanisms causing destabilization and resorption at rims of plagioclase crystals (i.e., changes of pressure, temperature, and/or volatile composition of the host melt; e.g., Streck, 2008 and references therein). Specifically, An and FeO do not correlate within sieve textures of crystals for the episode of the 3 December 2015; contrariwise, concomitant increase of An and FeO characterized the sieved zones of crystals emitted during the eruptions of 4 December 2015 and May 2016. The first type of zoning may form in response of changing oxygen fugacity conditions of the system, which controls the partitioning behavior of iron in plagioclase without affecting the major element composition (Giuffrida et al., 2017; Giuffrida & Viccaro, 2017; Nicotra & Viccaro, 2012; Sugawara, 2001; Viccaro et al., 2014; Wilke & Behrens, 1999). Episodes of gas flushing into the shallow magmatic reservoirs of Mt. Etna could likely explain changes in the magmatic redox conditions, and could be therefore considered as the main triggering mechanism for the eruption of 3 December 2015. Differently, processes of mafic recharge and mixing, with consequent incorporation of crystals into a recharging melt of more basic composition can lead to the development of sieved zones at the crystal rim coupled with concordant An and FeO increase, as shown by several experimental studies on the matter (Tsuchiyama, 1985). The dominance of such kind of sieve textures at the rim of crystals emitted during the eruptions of 4 December 2015 and May 2016 leads to the idea that the eruptive activity during these periods was dominantly triggered by replenishment with more basic, gas-rich magmas of the shallow portion of the Mt. Etna plumbing system.

A more detailed picture of the plumbing system dynamics that preceded the 2015–2016 activity at the VOR is drawn from the investigation of the chemical zoning of olivine crystals. Several studies investigating volcanic rocks emitted at Mt. Etna during past effusive and explosive eruptions focused on the compositional diversity of olivine cores which has led to the identification of compositionally distinct magmatic environments (hereafter indicated as M_i) beneath the volcano where crystals have resided and grown at definite chemical-physical conditions before emission (i.e., Giuffrida & Viccaro, 2017; Kahl et al., 2011, 2013, 2015, 2017). Specifically, combining geochemical data with thermodynamic modeling, Giuffrida and Viccaro (2017) detected five main magma environments, distributed across a pressure range between 650 and 30 MPa, which were variously reactivated during the eruptive episodes that occurred between 2011 and 2013. They are M_{00} which indicates the crystallization environment of the olivine cores at Fo_{84} (OP1) located in a pressure range of 650–550 MPa; M_0 which accounts for the crystallization of the $Fo_{80–82}$ olivine cores (OP2) at pressure of 420–380 MPa; M_{1a} (290–230 MPa) refers to crystals with Fo_{78} cores (OP3); M_{1b} designates a magmatic environment at 160–120 MPa where $Fo_{75–76}$ olivines (OP4) form; and the shallower M_2 environment (40–30 MPa) that accounts for crystals with $Fo_{70–73}$ core compositions (OP5). Routes of connection between these different environments and processes of intrusion and mixing that Etnean magmas underwent during ascent were inferred by these authors through the chemical zoning observed at the olivine rims. For example, the reverse zoning may indicate that crystals were involved in hybrid magmas originated by mafic recharge and mixing, and the normal zoning may be an expression of magma transfer and subsequent diffusive relaxation of the olivine zoning after intrusion into a more differentiated melt.

The compositional heterogeneities of the olivine cores in volcanic products of December 2015 and May 2016 erupted at VOR confirm the existence within the modern volcano plumbing system of five magmatic environments preserving chemical and physical characteristics very similar to those previously identified for the 2011–2013 activity at the NSEC. Definition of the physical parameters, such as P, T, and fO_2, associated with each environment in which the olivines form is based on the thermodynamic constraints provided by Giuffrida and Viccaro (2017) by simulating the evolutionary path of magmas in the period 2011–2013. This was made possible because products related to the eruptions of 2015 and 2016 have prominent similarity with compositions of the volcanic rocks erupted during the 2011–2013 period, and they both exhibit the most basic compositions erupted at Mt. Etna in recent times. This supports the hypothesis that the chemical-physical evolution of the melt involved in the recent activity at VOR has followed the same evolutionary path of the primitive melt that fed the 2011–2013 paroxysmal eruptions at the NSEC. Despite whole

rock compositions do not present any indication of magma rejuvenation from December 2015 to May 2016 (e.g., MgO, CaO are rather unvaried; supporting information Table S1), olivine chemistry highlights the presence of high-Mg Fo_{86-89} magmas that rose up from very deep regions of the Mt. Etna plumbing system (>650 MPa). Evidence of this mafic end-member is given by the reverse zoning patterns observed in most of the OP2 crystals erupted during the episode of 18–19 May 2016, showing Fo increase up to Fo_{89} at the rim, which reflect the interaction of the M_0 melt with a more primitive magma, hereafter M_x, whose equilibrium olivine must be more forsteritic than Fo_{84}. On the whole, normal and reverse zoning patterns in OP1, OP2, and OP4 crystals of 18–19 May eruptions indicate the reactivation of the deepest and more primitive reservoirs, such as the M_{00}, M_0, and M_{1b} (650–120 MPa). In contrast, the compositional range preserved in crystals from 3 to 5 December 2015, and from the late eruptive phase of May 2016 (i.e., episode of 21 May) supports the occurrence of multiple episodes of transfer, intrusion, and residence involving more differentiated magmatic end-members, mainly M_{1b} and M_2, located at shallow depth beneath the volcano. For the episodes of 3–5 December 2015, processes of magma exchange between M_0 and M_{1b} reservoirs are given by both the reverse zoning patterns of OP4 olivines (Fo_{75-76}) with Fo concentration increases to Fo_{80}, and by the normally zoned rims of OP2, where the Fo contents declines to $\sim Fo_{75}$. Finally, olivine populations crystallizing from M_0 and M_{1b} record direct transfer histories to the most differentiated M_2 environment (Fo_{70-73}, ~30 MPa). Here the arrival of magmas with different degrees of differentiation from deeper levels of the plumbing system caused the reverse zoning that characterizes the rim of OP5 crystals (Fo_{70-73}). Eruptions occurring during this period are likely direct consequences of these recharge and mixing processes within the more evolved shallow storage zone (at ~1–2 km of depth), from which magmas rise directly to the surface. Clear evidence of this hypothesis is that OP5 olivines generally do not record any subsequent normal zoning at the outermost rim, a feature that reflects relatively fast migration of magma to the surface.

Similar processes of replenishment of the shallow M_2 environment with the M_0 and M_{1b} magmas have been also identified through the compositional range preserved in crystals from the late phase of volcanic activity in May 2016 (episode of May 21). Olivines of the 21 May 2016 eruption are indeed typified by two dominant zoning types (reverse zoning up to Fo_{76} at the OP5 crystal rims, and normal zoning with Fo decreasing to Fo_{73} in OP2 crystals). This feature clearly suggests a main connection route between the M_0, M_{1b}, and M_2 storage zones, allowing the transfer of mafic magma (Fo_{80-82}) to the surface. Normal zoning in a few OP1 crystals (Fo_{83-84}), with Fo decreasing at rim to Fo_{74-75}, evidences minor connections between the deeper magmatic environments M_{00} and M_{1b}.

Quantifying the time scales of magma residence, intrusion, and mixing is crucial for the development of models of magma emplacement, remobilization, and eruption at active volcanoes. Temporal constraints of the magma dynamics within the distinct storage zones defined by chemical record of olivine before the eruptions of December 2015 and May 2016 at VOR are provided by modeling the diffusive relaxation through time of normal and reverse zoning patterns in olivine crystals, which are both the expression of changed initial thermodynamic conditions. The diffusion model adopted in this study follows the approach of Costa et al. (2008) and Costa and Morgan (2010), which use Fick's law-based diffusion equations and concentration-dependent diffusion coefficients ($D_{Fe\text{-}Mg}$). The measured compositions at the rim of crystals were fixed as boundary conditions. To reduce the uncertainties on time calculation due to the olivine anisotropy, crystals were selected by considering their section orientation with respect to the fast diffusion direction (*c* axis). Criteria of selection of the crystals suitable for modeling calculation, together with the modeling strategy are the same as those described in Giuffrida and Viccaro (2017). Fe-Mg diffusion coefficients were at first determined along [001] of olivine crystals by using formulas of Dohmen and Chakraborty (2007), and finally they were corrected for the orientation of the compositional traverse with respect to the crystallographic *a*, *b*, and *c* axis. Coefficients were calculated for each OP population by using the *T*, *P*, and fO_2 parameters characterizing the corresponding environments that were determined through the MELTS simulations (Giuffrida & Viccaro, 2017). The results of diffusion modeling are available in the supporting information Table S4.

The spectrum of time scales determined by diffusion modeling covers a time span that ranges from 4 to 240 days, with the majority (~90%) of the recorded time scales of residence and mixing that are confined within 2 months before eruption. Diffusion modeling calculations on the reverse zoning patterns of OP2 (Fo_{80-82}) olivines found in products of 18–19 May 2016 eruptions provide very short time scales of 4–5 days

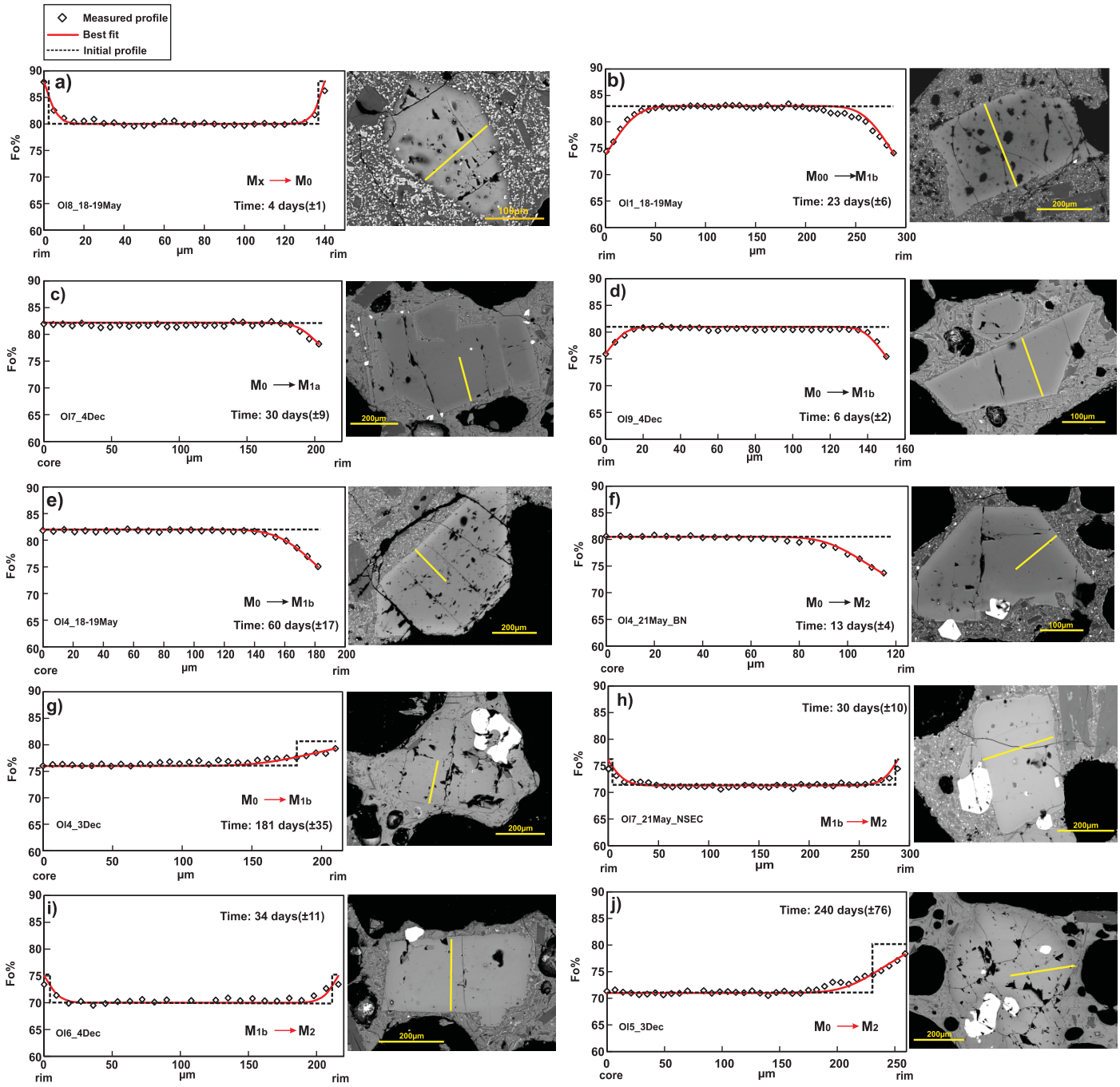

Figure 9. Fe-Mg diffusion modeling for representative olivine crystals found in erupted products of the December 2015 and May 2016 activity. The type of connection between the Mi involved is indicated for each diagram (black arrow: intrusion; red arrow: mixing). Time scales and related uncertainties calculated by the diffusion model are reported. The best fit for diffusion curves is represented by the red lines, whereas black and dashed lines indicate the initial concentration profile prior to the diffusion.

for the deep mixing episodes involving the M_0 and the more basic M_x magma (Figure 9a). However, given that these OP2 crystals display resorption at the rim, the derived time scales must be considered cautiously as they do not furnish the entire timing between the mixing process and the eruption. Intrusion of M_{00} magma into M_{1b} is evidenced by OP1 crystals found in May products, whose estimated time scales covers a range of 5–23 days (Figure 9b). OP2 olivines record processes of migration and intrusion of the M_0 ($Fo_{80–82}$) magma toward the more differentiated environments M_{1a} (Fo_{78}) and M_{1b} ($Fo_{75–76}$) prior to eruptions of December 2015. Based on our calculation, the chemical zoning of the OP2 crystals ($Fo_{80–82}$) requires on

average 10–30 days to relax through diffusion to the Fo_{78} composition after intrusion of M_0 into the M_{1a} reservoir (290–230 MPa; Figure 9c), whereas for the intrusion and residence into M_{1b} (160–120 MPa), we derived time scales of 6 days for December 2015 (Figure 9d). Intrusion of M_0 into M_{1b} and M_2 reservoirs prior to eruptions of May 2016 occurred, respectively, in 60 days (Figure 9e) and 8–22 days (Figure 9f). The reverse zoning recorded at the rim of OP4 (Fo_{75-76}) crystals provide further evidence of interaction and mixing between M_0 and M_{1b} melts, a process that probably occurred ~140–181 days before the eruptive episodes of December 2015 (Figure 9g). OP5 (Fo_{70-73}) reverse zoning reveal low pressure episodes of recharge with M_{1b} magma that affected the shallower M_2 (Fo_{70-73}; 40–30 MPa) environment over the whole period under investigation. These processes occur over a range of time scales varying from 8 to 45 days (Figures 9h and 9i). A single reverse-zoned OP5 crystal from the 3 December 2015 eruption indicates interaction of M_2 with M_0 magma ~240 days before the first paroxysmal event in December 2015 (Figure 9j).

Uncertainties on time scale determinations were calculated by using standard procedures for error propagation in the Arrhenius expression for calculation of the diffusion coefficients (D), following the method described by Kahl et al. (2015). For the error propagation analysis, uncertainties on temperatures and fO_2 of crystallization of each olivine population were $\sigma_T = 10°C$ and $\sigma_{\log fO2} = 0.25$, respectively. These uncertainties lead to a propagated uncertainty on the calculated time scales that ranges from ±1 days for the shorter time scales to ±76 days for the longer time scales.

5.3. An Integrated Model for Magma Storage and Dynamics

The combination of geodetic, seismic, infrasonic, and petrological data allowed us to draw a general picture of dynamics of magmas that have fed the activity at VOR crater during December 2015 and May 2016 (Figure 10). The compositional heterogeneities of crystals highlighted the presence of magmas at distinct differentiation degrees that migrate to the surface through multiple episodes of intrusion and residence at distinct depths within the multilevel Etnean plumbing system.

Assuming a lithostatic pressure gradient of 27 MPa/km for Mt. Etna (Corsaro & Pompilio, 2004), we find that storage depths of these magmatic environments match well with locations of seismic and geodetic signals (Figure 10). Specifically, on the basis of seismic data the storage depth of the shallowest and more evolved (Fo_{70-73}) M_2 magma falls in the spatial range defined by volcanic tremor and LP event locations (1–3 km asl). Ground deformation data also indicate the presence of a magmatic source at depth of 4.9–5.7 km bsl, which is rather consistent with the depth of storage of the M_{1b} reservoir (Fo_{75-76}) defined by petrological investigations.

The presence of deeper magmatic environments such as M_{1a} (Fo_{78}), M_0 (Fo_{80-82}), and M_{00} (Fo_{83-84}) was not detected by the geophysical data presented in this study. However, evidence of these reservoirs is provided by several geophysical observations collected over the last decades. For instance, M_{1a} (7.5–10 km bsl) well matches with a magmatic reservoir that fed the 2001 and 2002–2003 eruptions (see Palano et al., 2017 and references therein). This reservoir has been only occasionally detected during the last two decades (e.g., Cannata et al., 2015; Palano et al., 2008). M_0 (13–15 km bsl) roughly coincides with the magmatic sources related to the long-term uplift of the volcano edifice, as proposed in De Guidi et al. (2014). The presence of M_{00} (19–23 km bsl) and M_x (>25 km) can be related to the *P* wave low-velocity anomalies found beneath Mt. Etna and associated with the deep portion of the volcano feeding system by Monna et al. (2013). It is also worth noting that the storage depths of these more mafic reservoirs fall in the same crustal range (i.e., 20–30 km bsl) affected by low to moderate magnitude seismic sequences ($M < 3.5$) during the period October–November 2015 and March–April 2016. Such a phenomenon is not new at Mt. Etna, where deep VT earthquakes have been often interpreted as earlier markers of future volcanic activity (Castellano et al., 1993; Gresta et al., 1990; Patanè et al., 2004).

Our geophysical and petrological results show that both the investigated eruptive periods (December 2015 and May 2016) were preceded by episodes of mafic replenishment from the deep portions of the volcano plumbing system, and eventually mixing that occurred shortly before the eruptions (i.e., only a few months based on petrological data), producing phenomena of pressurization in different portions of the plumbing system. In this regard, inflation patterns of the ground deformation data indicate that the magmatic reservoir M_{1b} was pressurized since June 2015 (T1). The reverse zoning patterns of OP4 crystals (Fo_{75-76}) suggests that such a pressurization occurred as a response to interaction between M_0 and M_{1b} melts ~140–181 days before the eruptions of December 2015. In the same period, we recorded a gradual increase in amplitude of

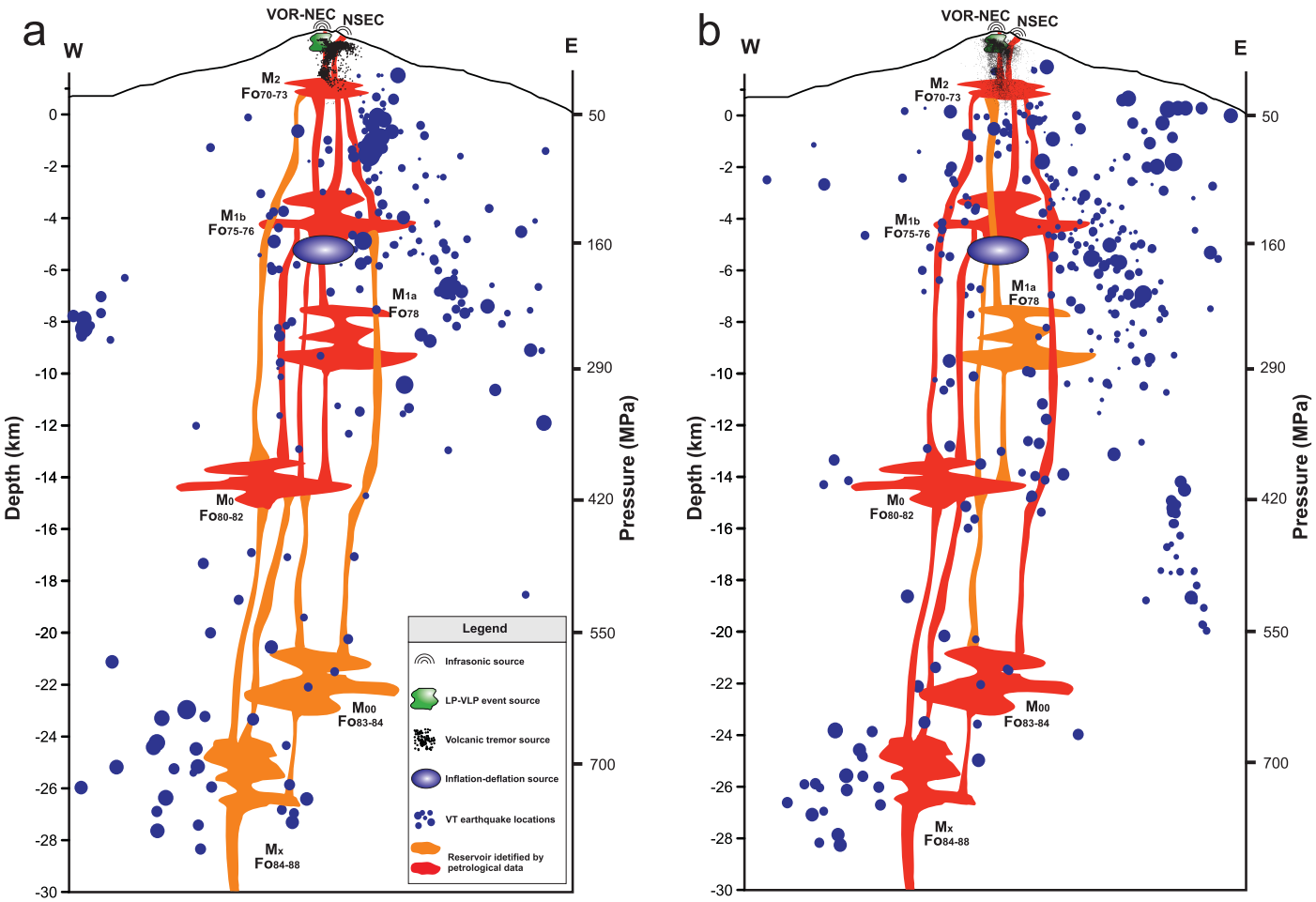

Figure 10. W-E section of Mt. Etna with a schematic model of plumbing system showing infrasonic sources, LP-VLP source volume, volcanic tremor centroids, VT earthquake locations, inflation-deflation geodetic sources, and the magmatic environments identified by petrological data (see legend in the right bottom corner of "a"). (a) Volcanic tremor centroids, VT earthquakes locations, and main magmatic environments (in red) highlighted during June–December 2015 (months preceding the first eruptive period), while the magmatic environments detected during December 2015 to May 2016 are represented in orange. (b) Volcanic tremor centroids, VT earthquakes locations, and main magmatic environments (in red) highlighted during December 2015 to August 2016 (months preceding, accompanying and following the second eruptive period), while the magmatic environments detected during June–December 2015 are represented in orange. It must be underlined that this sketch model shows only the depth relationships between portions of plumbing system detected by geophysical analyses and magmatic environments evidenced by petrological data. Both geometry of magmatic environments and horizontal relationships are only indicative.

both volcanic tremor and LP events in the shallowest portion of the volcano plumbing system in correspondence of the M_2 reservoir. Moreover, a clear change in the patterns of both LP amplitude and volcanic tremor RMS amplitudes occurred since 1 November 2015, at the same time as a strong explosion, interpreted as a plug expulsion at one of the summit craters. Such a change probably occurred as a response of the intrusion by more mafic and volatile-rich magma into the M_2 reservoir, recorded by the OP5 (Fo_{70-73}) crystals with reverse zoning, which happened about 1 month before the paroxysmal events of December 2015. Petrological data also indicate that deep magma migration from M_0 to M_{1a} and M_{1b} reservoirs occurred within the same time interval before the December 2015 eruptions. The occurrence of this mafic intrusion is likely responsible for the concomitant increase of both SO_2/HCl and SO_2 compositions in the gas plume detected a few weeks before the resumption of volcanic activity at VOR crater (Corsaro et al., 2017). The release of volatiles from the ascending magma into shallow reservoirs could have played a primary role in triggering the first paroxysmal event, as suggested by textural and compositional features at the rims of plagioclase crystals from the 3 December 2015 samples. Longer time scales derived from olivine diffusion modeling (up to 240 days) put into evidence the involvement of residing magma during the first phase of December 2015 activity.

On the basis of our geodetic data, the eruptive events that occurred during early December 2015 were accompanied by a vigorous deflation (T2) related to the fast depressurization of the apical portion of M_{1b} as a consequence of gas discharge and magma withdrawal. In this regard, on the basis of data from three borehole strainmeters, Bonaccorso and Calvari (2017) have found that the eruptive sequence of 3–5 December 2015 was characterized by a decreasing volume ratio fluid/pyroclastic from the first eruption to the fourth and last one. They suggested a source located at ~1.5–1.8 km bsl, which is significantly shallower than M_{1b} fixed on the basis of our geodetic and petrological constraints. Such a difference could be due to the different used instrumental data. In fact, the three borehole strainmeters are located on the middle to upper western flank of the volcano at distances from the summit area larger than 4.8 km. On the contrary, the GPS network covers all the volcano slopes, thus providing a dense sampling (especially closely to the summit volcanic area) of the observed deformation field (Figure 1). Furthermore, our proposed model encompasses all the four powerful paroxysmal episodes, therefore inferring the cumulative effect at the end of the whole paroxysmal sequence as a consequence of the magmatic fluid withdrawal from the feeding reservoir. Conversely, Bonaccorso and Calvari (2017) focused on strain changes related to each eruptive episode, therefore taking also into account possible deformation transients related to magma motion along the shallower portion of the plumbing system, neglecting the partial recovery after the end of each paroxysm.

The M_{1b} reservoir starts to be pressurized again a few days after the end of eruptions of December 2015. This was accompanied by the pressurization of M_2, which is testified by the gradual increase of volcanic tremor amplitude that continued until May 2016. In particular, we recorded a more prominent increase in volcanic tremor amplitude since the end of March 2016. This is likely related to the beginning of replenishment of the M_2 reservoir, which occurred about 1 month before the eruption of 18 May 2016 according to our olivine diffusion modeling calculations. Such a pressurizing phenomenon of the shallow part of the magmatic plumbing system may be the consequence of the pressure drop in M_{1b} after magma withdrawal toward M_2. This would have created a pressure imbalance between M_{1b} and the deepest reservoirs, therefore promoting ascent of fresh, more basic magmas from depth. Petrological data confirm that the volcanic activity during May 2016 was driven by the reactivation of the most basic and deepest magma reservoirs (i.e., M_x, M_{00}, and M_0). The obtained time scales also highlight very rapid processes of magma transfer toward the shallow crustal levels, i.e., within 1–6 weeks before the beginning of the May 2016 eruptions, which are on the whole faster than those observed before the December 2015 eruptions. The faster ascent of basic magma before the eruptions of May 2016 could also explain the rather unchanged whole rock compositions throughout the 2015–2016 period. Indeed, this could be a consequence of incomplete homogenization due to the short time scale of magma mixing. Fast dynamics of replenishment and ascent of mafic magma have been observed at Mt. Etna also for other recent eruptive events (Giuffrida et al., 2018; Giuffrida & Viccaro, 2017; Ubide & Kamber, 2018). This links very well with previous studies pointing to progressive mafic intrusion of deep undegassed magma into the plumbing system during the last decades, and to the high efficiency of the mafic magma as an eruption trigger at Mt. Etna.

6. Conclusions

The integrated analysis of geodetic, seismic, and petrological data applied to a complex volcanic system like Mt. Etna has proved to be a powerful tool to gain insights on the spatial and temporal history of magma transfer and recharge beneath the volcano. The complex data set presented in this study allowed definition of the spatial distribution of the main magmatic environments beneath Mt. Etna and gave us important insights on their reactivation modes leading to resumption of the activity at the VOR crater during 2015–2016. Paroxysmal episodes of December 2015 and May 2016 have been rather similar for what concerns the eruptive behavior and compositions of emitted products. Indeed, both the eruptive periods were preceded by pressurization phenomena in shallow and intermediate portions of plumbing system (evidenced by ground deformation data, volcanic tremor, and LP events), as well as by activation of distinct magmatic environments in the preceding days-months (suggested by petrological data). Although geodetic and seismic data provided evidence on the pressurization/depressurization of the same portions of the plumbing system, core-to-rim chemical profiles of plagioclase and olivine crystals in the emitted products highlighted some differences in the storage and transfer dynamics of magmas that have fed these eruptions. There are indications that the 2015 eruptions have been fed by magmas stored at intermediate-shallow levels of the

plumbing system (160–30 MPa) that were pushed upward as a response of magma injections from deeper reservoirs. During 2016, the activity was mainly driven by the ascent of basic magmas coming from the deepest levels of the Etnean storage zones (>600 MPa) and their chemical interaction with magmas residing in shallow reservoirs. One of the main findings of this work is detection of very deep magma replenishment, never observed after the 2001 eruption at the volcano. Furthermore, through diffusion modeling of the olivine chemical zoning, we have found that these deep magmas were brought to shallow crustal levels in very short time scales (~1 month).

This study highlights that the trigger of unusual, highly energetic eruptions at Mt. Etna volcano is often strictly related to the fast ascent of deep, undegassed magmas. Awareness of the dynamics governing such kind of eruptions and their time scales is therefore crucial for a correct evaluation and management of the hazard associated with the paroxysmal activity at Mt. Etna as well as at other volcanic systems able to produce eruptions where basic magma is involved.

Acknowledgments
We are indebted to the technicians of the INGV, Osservatorio Etneo for enabling the acquisition of seismic, infrasonic and GPS data. A.C. thanks the project ICE-VOLC (PNRA14_00011) funded by Programma Nazionale Ricerche in Antartide. This work has been also supported by the funding programs of the University of Catania through the FIR 2014 grant number 2F119B and PRA 2016-18 cod. 22722132120 (Project Coordinator M. Viccaro). We thank Ulrich Faul for the editorial handling of the manuscript, Teresa Ubide and an anonymous reviewer for their useful suggestions. Geochemical and petrological data used in this paper are available in the supporting information. Conversely, the other data are available from the authors as follows, GPS: mimmo.palano@ingv.it; seismic: giuseppe.digrazia@ingv.it; infrasonic: mariangela.sciotto@ingv.it, in agreement with the INGV data policy.

References

Allegre, C. J., Provost, A., & Jaupart, C. (1981). Oscillatory zoning: A pathological case of crystal growth. *Nature*, *294*, 223–228.

Aloisi, M., Jin, S., Pulvirenti, F., & Scaltrito, A. (2017). The December 2015 Mount Etna eruption: An analysis of inflation/deflation phases and faulting processes. *Journal of Geodynamics*, *107*, 34–45.

Behncke, B., Branca, S., Corsaro, R. A., De Beni, E., Miraglia, L., & Proietti, C. (2014). The 2011–2012 summit activity of Mount Etna: Birth, growth and products of the new SE crater. *Journal of Volcanology and Geothermal Research*, *270*, 10–21.

Blundy, J., & Cashman, K. V. (2008). Petrologic reconstruction of magmatic system variables and processes. *Review in Mineralogy and Geochemistry*, *69*, 179–239.

Bonaccorso, A., & Calvari, S. (2017). A new approach to investigate an eruptive paroxysmal sequence using camera and strainmeter networks: Lessons from the 3–5 December 2015 activity at Etna volcano. *Earth and Planetary Science Letters*, *475*, 231–241.

Cannata, A., Di Grazia, G., Aliotta, M., Cassisi, C., Montalto, P., & Patanè, D. (2013). Monitoring seismo-volcanic and infrasonic signals at volcanoes: Mt. Etna case study. *Pure and Applied Geophysics*, *170*, 1751–1771.

Cannata, A., Hellweg, M., Di Grazia, G., Ford, S., Alparone, S., Gresta, S., et al. (2009). Long period and very long period events at Mt. Etna volcano: Characteristics, variability and causality, and implications for their sources. *Journal of Volcanology and Geothermal Research*, *187*, 227–249.

Cannata, A., Spedalieri, G., Behncke, B., Cannavò, F., Di Grazia, G., Gambino, S., et al. (2015). Pressurization and depressurization phases inside the plumbing system of Mount Etna volcano: Evidence from a multiparametric approach. *Journal of Geophysical Research: Solid Earth*, *120*, 5965–5982. https://doi.org/10.1002/2015JB012227

Castellano, M., Ferrucci, F., Godano, C., Imposa, S., & Milano, G. (1993). Upwards migration of seismic focii: A forerunner of the 1989 eruption of Mt Etna (Italy). *Bulletin of Volcanology*, *55*(5), 357–361.

Chouet, B. A., & Matoza, R. S. (2013). A multi-decadal view of seismic methods for detecting precursors of magma movement and eruption. *Journal of Volcanology and Geothermal Research*, *252*, 108–175.

Corsaro, R. A., Andronico, D., Behncke, B., Branca, S., Caltabiano, T., Ciancitto, F., et al. (2017). Monitoring the December 2015 summit eruptions of Mt. Etna (Italy): Implications on eruptive dynamics. *Journal of Volcanology and Geothermal Research*, *341*, 56–69.

Corsaro, R. A., & Pompilio, M. (2004). Buoyancy-controlled eruption of magmas at Mt Etna. *Terra Nova*, *16*(1), 16–22.

Costa, F., Dohmen, R., & Chakraborty, S. (2008). Timescales of magmatic processes from modeling the zoning patterns of crystals. In K. D. Putirka & F. J. Tepley III (Eds.), *Minerals, inclusions and volcanic processes, reviews in mineralogy and geochemistry* (pp. 545–594). Chantilly, VA: Mineralogical Society of America.

Costa, F., & Morgan, D. J. (2010). Time constraints from chemical equilibration in magmatic crystals. In A. Dosseto (Ed.), *Timescales of magmatic processes: From core to atmosphere* (pp. 125–159). West Sussex, UK: John Wiley.

Davidson, J. P., Morgan, D. J., Charlier, B. L. A., Harlou, R., & Hora, J. M. (2007). Microsampling and isotopic analysis of igneous rocks: Implications for the study of magmatic systems. *Annual Reviews of Earth and Planetary Sciences*, *35*, 273–311.

Davidson, J. P., Tepley, F., III, Palacz, Z., & Meffan-Main, S. (2001). Magma recharge, contamination and residence times revealed by in situ laser ablation isotopic analysis of feldspar in volcanic rocks. *Earth and Planetary Science Letters*, *184*, 427–442.

De Guidi, G., Imposa, S., Scudero, S., & Palano, M. (2014). New evidence for Late Quaternary deformation of the substratum of Mt. Etna volcano (Sicily, Italy): Clues indicate active crustal doming. *Bulletin of Volcanology*, *76*(5), 816.

Di Grazia, G., Falsaperla, S., & Langer, H. (2006). Volcanic tremor location during the 2004 Mount Etna lava effusion. *Geophysical Research Letters*, *33*, L04304. https://doi.org/10.1029/2005GL025177

Dohmen, R., & Chakraborty, S. (2007). Fe-Mg diffusion in olivine II: Point defect chemistry, change of diffusion mechanisms and a model for calculation of diffusion coefficients in natural olivine. *Physics and Chemistry of Minerals*, *34*, 409–430.

Druitt, T., Costa, F., Deloule, E., Dungan, M., & Scaillet, B. (2012). Decadal to monthly timescales of magma transfer and reservoir growth at a caldera volcano. *Nature*, *482*, 77–82.

Dzurisin, D. (2007). *Volcano deformation: Geodetic monitoring techniques*. Berlin, Germany: Springer Praxis.

Efron, B. (1982). *The jackknife, the bootstrap and other resampling plans*. Philadelphia, PA: Society for Industrial and Applied Mathematics.

Fee, D., Haney, M. M., Matoza, R. S., Van Eaton, A. R., Cervelli, P., Schneider, D. J., et al. (2017). Volcanic tremor and plume height hysteresis from Pavlof Volcano, Alaska. *Science*, *355*, 45–48.

Gambino, S., Cannata, A., Cannavò, F., La Spina, A., Palano, M., Sciotto, M., et al. (2016). The unusual 28 December 2014 dike-fed paroxysm at Mount Etna: Timing and mechanism from a multidisciplinary perspective. *Journal of Geophysical Research: Solid Earth*, *121*, 2037–2053. https://doi.org/10.1002/2015JB012379

Giuffrida, M., Holtz, F., Vetere, F. P., & Viccaro, M. (2017). Effects of CO_2 flushing on crystal textures and compositions: Experimental evidence from recent K-trachybasalts erupted at Mt. Etna. *Contributions to Mineralogy and Petrology*, *172*(11–12), 90. https://doi.org/10.1007/s00410-017-1408-3

Giuffrida, M., & Viccaro, M. (2017). Three years (2011–2013) of eruptive activity at Mt. Etna: Working modes and timescales of the modern volcano plumbing system from micro-analytical studies of crystals. *Earth-Science Reviews*, *171*, 289–322.

Giuffrida, M., Viccaro, M., & Ottolini, L. (2018). Ultrafast syn-eruptive degassing and ascent trigger high-energy basic eruptions. *Scientific Reports*, *8*(1), 147. https://doi.org/10.1038/s41598-017-18580-8

Gonzalez, P. J., & Palano, M. (2014). Mt. Etna 2001 eruption: New insights into the magmatic feeding system and the mechanical response of the western flank from a detailed geodetic dataset. *Journal of Volcanology and Geothermal Research*, *274*, 108–121.

Gresta, S., Longo, V., & Viavattene, A. (1990). Geodynamic behavior of eastern and western sides of Mount Etna. *Tectonophysics*, *179*, 81–92.

Gruppo Analisi Dati Sismici. (2017). *Catalogo dei terremoti della Sicilia Orientale—Calabria Meridionale (1999–2017)*. INGV-Catania. Retrieved from http://www.ct.ingv.it/ufs/analisti/catalogolist.php

Herring, T. A., King, R. W., & McClusky, S. C. (2015). *Introduction to GAMIT/GLOBK, release 10.4*. Cambridge: Massachusetts Institute of Technology.

Kahl, M., Chakraborty, S., Costa, F., & Pompilio, M. (2011). Dynamic plumbing system beneath volcanoes revealed by kinetic modeling, and the connection to monitoring data: An example from Mt. Etna. *Earth and Planetary Science Letters*, *308*, 11–22.

Kahl, M., Chakraborty, S., Costa, F., Pompilio, M., Liuzzo, M., & Viccaro, M. (2013). Compositionally zoned crystals and real-time degassing data reveal changes in magma transfer dynamics during the 2006 summit eruptions of Mt. Etna. *Bulletin of Volcanology*, *75*(2), 692. https://doi.org/10.1007/s00445-013-0692-7

Kahl, M., Chakraborty, S., Pompilio, M., & Costa, F. (2015). Constraints on the nature and evolution of the magma plumbing system of Mt. Etna volcano (1991–2008) from a combined thermodynamic and kinetic modelling of the compositional record of minerals. *Journal of Petrology*, *56*(10), 2025–2068.

Kahl, M., Viccaro, M., Ubide, T., Morgan, D., & Dingwell, D. B. (2017). A branched magma feeder system during the 1669 eruption of Mt. Etna: Evidence from a time-integrated study of zoned olivine phenocryst populations. *Journal of Petrology*, *58*(3), 443–472.

Kao, H., & Shan, S. J. (2004). The source-scanning algorithm: Mapping the distribution of seismic sources in time and space. *Geophysical Journal International*, *57*, 589–594.

Mattia, M., Bruno, V., Caltabiano, T., Cannata, A., Cannavò, F., D'Alessandro, W., et al. (2015). A comprehensive interpretative model of slow slip events on Mt. Etna's eastern flank. *Geochemistry Geophysics Geosystems*, *16*, 635–658. https://doi.org/10.1002/2014GC005585

McNutt, S. R. (2005). Volcanic seismology. *Annual Reviews of Earth and Planetary Sciences*, *33*(1), 461–491.

McNutt, S. R., Thompson, G., Johnson, J. B., Angelis, D., S., & Fee, D. (2015). Seismic and infrasound monitoring. In H. Sigurdsson (Ed.), *The encyclopedia of volcanoes* (2nd ed., pp. 1071–1099). Amsterdam, the Nethwrlands: Elsevier.

Monna, S., Sgroi, T., & Dahm, T. (2013). New insights on volcanic and tectonic structures of the southern Tyrrhenian (Italy) from marine and land seismic data. *Geochemistry Geophysics Geosystems*, *14*, 3703–3719. https://doi.org/10.1002/ggge.20227

Moran, S. C., Malone, S. D., Qamar, A. I., Thelen, W. A., Wright, A. K., & Caplan-Auerbach, J. (2008). Seismicity associated with the renewed dome-building eruption of Mount St. Helens 2004–2005. In D. R. Sherrod. (Ed.), *A volcano rekindled: The renewed eruption of Mount St. Helens, 2004–2006* (Prof. Pap. 1750, pp. 27–54). Reston, VA: U.S. Geological Survey.

Nelson, S. T., & Montana, A. (1992). Sieve textured plagioclases in volcanic rocks produced by rapid decompression. *American Mineralogist*, *77*, 1242–1249.

Nicotra, E., & Viccaro, M. (2012). Transient uprise of gas and gas-rich magma batches fed the pulsating behaviour of the 2006 eruptive episodes at Mt. Etna volcano. *Journal of Volcanology and Geothermal Research*, *227–228*, 102–118.

Palano, M., Puglisi, G., & Gresta, S. (2008). Ground deformation patterns at Mt. Etna from 1993 to 2000 from joint use of InSAR and GPS techniques. *Journal of Volcanology and Geothermal Research*, *169*(3–4), 99–120. https://doi.org/10.1016/j.jvolgeores.2007.08.014

Palano, M., Rossi, M., Cannavò, F., Bruno, V., Aloisi, M., Pellegrino, D., et al. (2010). Etn@ref, a geodetic reference frame for Mt. Etna GPS networks. *Annals of Geophysics*, *53*(4), 48–79.

Palano, M., Viccaro, M., Zuccarello, F., & Gresta, S. (2017). Magma transport and storage at Mt. Etna (Italy): A review of geodetic and petrological data for the 2002-03, 2004 and 2006 eruptive events. *Journal of Volcanology and Geothermal Research*, *347*, 149–164. https://doi.org/10.1016/j.jvolgeores.2017.09.009

Pallister, J., & McNutt, S. R. (2015). Synthesis of volcano monitoring. In: H. Sigurdsson (Ed.), *The encyclopedia of volcanoes* (2nd ed., pp. 1151–1171). Amsterdam, the Netherlands: Elsevier.

Patanè, D., Aiuppa, A., Aloisi, M., Behncke, B., Cannata, A., Coltelli, M., et al. (2013). Insights into magma and fluid transfer at Mount Etna by a multiparametric approach: A model of the events leading to the 2011 eruptive cycle. *Journal of Geophysical Research*, *118*, 3519–3539. https://doi.org/10.1002/jgrb.50248

Patanè, D., Cocina, O., Falsaperla, S., Privitera, E., & Spampinato, S. (2004). Mt. Etna volcano: A seismological framework. In: S. Calvari (Ed.), *The Mt. Etna volcano* (pp. 147–165). Washington, DC: American Geophysical Union.

Patanè, D., Di Grazia, G., Cannata, A., Montalto, P., & Boschi, E. (2008). Shallow magma pathway geometry at Mt. Etna volcano. *Geochemistry Geophysics Geosystems*, *9*, Q12021. https://doi.org/10.1029/2008GC002131

Ripepe, M., Bonadonna, C., Folch, A., Donne, D. D., Lacanna, G., Marchetti, E., et al. (2013). Ash-plume dynamics and eruption source parameters by infrasound and thermal imagery: The 2010 Eyjafjallajökull eruption. *Earth and Planetary Science Letters*, *366*, 112–121.

Sciotto, M., Cannata, A., Gresta, S., Privitera, E., & Spina, L. (2013). Seismic and infrasound signals at Mt. Etna: Modelling of North-East crater conduit and its relation with the feeding system of the 2008–2009 eruption. *Journal of Volcanology and Geothermal Research*, *254*, 53–68.

Spampinato, L., Sciotto, M., Cannata, A., Cannavò, F., La Spina, A., Palano, M., et al. (2015). Multiparametric study of the February–April 2013 paroxysmal phase of Mt. Etna New South-East crater. *Geochemistry Geophysics Geosystems*, *16*, 1932–1949. https://doi.org/10.1002/2015GC005795

Spina, L., Cannata, A., Privitera, E., Vergniolle, S., Ferlito, C., Gresta, S., et al. (2015). Insights into Mt. Etna's shallow plumbing system from the analysis of infrasound signals, August 2007 - December 2009. *Pure and Applied Geophysics*, *172*, 473–490.

Streck, M. J. (2008). Mineral textures and zoning as evidence for open system processes. In K. D. Putirka & F. J. Tepley III (Eds.), *Minerals, inclusions and volcanic processes, reviews in mineralogy and geochemistry* (pp. 595–622). Chantilly, VA: Mineralogical Society of America.

Sugawara, T. (2001). Ferric iron partitioning between plagioclase and silicate liquid: Thermodynamics and petrological applications. *Contributions to Mineralogy and Petrology*, *141*(6), 659–686.

Tarasewicz, J., White, R. S., Brandsdottir, B., & Schoonman, C. M. (2014). Seismogenic magma intrusion before the 2010 eruption of Eyjafjallajökull volcano, Iceland. *Geophysical Journal International*, *198*(2), 906–921.

Tiampo, K. F., Rundle, J. B., Fernandez, J., & Langbein, J. O. (2000). Spherical and ellipsoidal volcanic sources at Long Valley caldera, California, using a genetic algorithm inversion technique. *Journal of Volcanology and Geothermal Research*, *102*, 189–206.

Tsuchiyama, A. (1985). Dissolution kinetics of plagioclase in the melt of the system diopside albite-anorthite, and the origin of dusty plagioclase in andesites. *Contributions to Mineralogy and Petrology*, *89*(1), 1–16.

Ubide, T., & Kamber, B. S. (2018). Volcanic crystals as time capsules of eruption history. *Nature Communications*, *9*(1), 326. https://doi.org/10.1038/s41467-017-02274-w

Varley, N., Arámbula-Mendoza, R., Reyes-Dávila, G., Stevenson, J., & Harwood, J. (2010). Long-period seismicity during magma movement at Volcán de Colima. *Bulletin of Volcanology*, *72*, 1093–1107.

Viccaro, M., Barca, D., Bohrson, W. A., D'Oriano, C., Giuffrida, M., Nicotra, E., et al. (2016b). Crystal residence times from trace element zoning in plagioclase reveal changes in magma transfer dynamics at Mt. Etna during the last 400 years. *Lithos*, *248–251*, 309–323.

Viccaro, M., Calcagno, R., Garozzo, I., Giuffrida, M., & Nicotra, E. (2015). Continuous magma recharge at Mt. Etna during the 2011–2013 period controls the style of volcanic activity and compositions of erupted lavas. *Mineralogy and Petrology*, *109*, 67–83.

Viccaro, M., Garozzo, I., Cannata, A., Di Grazia, G., & Gresta, S. (2014). Gas burst vs. gas-rich magma recharge: A multidisciplinary study to reveal factors controlling duration of the recent paroxysmal eruptions at Mt. Etna. *Journal of Volcanology and Geothermal Research*, *278–279*, 1–13.

Viccaro, M., Giacomoni, P. P., Ferlito, C., & Cristofolini, R. (2010). Dynamics of magma supply at Mt. Etna volcano (Southern Italy) as revealed by textural and compositional features of plagioclase phenocrysts. *Lithos*, *116*(1–2), 77–91.

Viccaro, M., Zuccarello, F., Cannata, A., Palano, M., & Gresta, S. (2016a). How a complex basaltic volcanic system works: Constraints from integrating seismic, geodetic, and petrological data at Mount Etna volcano during the July–August 2014 eruption. *Journal of Geophysical Research: Solid Earth*, *121*, 5659–5678. https://doi.org/10.1002/2016JB013164

Wilke, M., & Behrens, H. (1999). The dependence of the partitioning of iron and europium between plagioclase and hydrous tonalitic melt on oxygen fugacity. *Contributions to Mineralogy and Petrology*, *137*, 102–114.

Williams, C. A., & Wadge, G. (2000). An accurate and efficient method for including the effects of topography in three-dimensional elastic models of ground deformation with applications to radar interferometry. *Journal of Geophysical Research*, *105*(B4), 8103–8120.

Yang, X. M., Davis, P. M., & Dieterich, J. H. (1988). Deformation from inflation of a dipping finite prolate spheroid in an elastic half-space as a model for volcanic stressing. *Journal of Geophysical Research*, *93*(B5), 4249–4257.